ACS APPLIED MATERIALS & INTERFACES

www.acsami.org

Research Article

Boswellic Acid-Integrated Chitosan Hybrid Nanogels for pH-Responsive Sustained Sunitinib Release and Lung Tumor Suppression

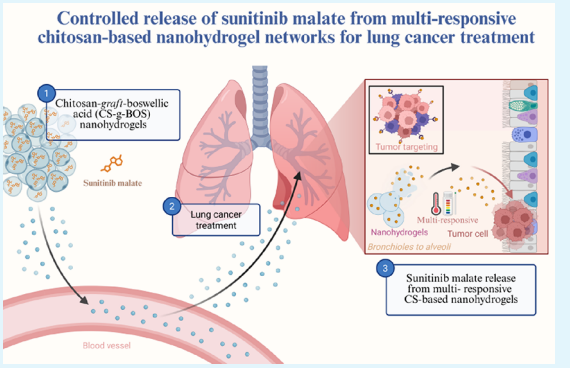
Zahra Amiri, Mehdi Jahanbakhshi, Mohsen Momeni, Ehsan Heidary, Shaghayegh AdibAmini, Tara Hassani Goodarzi, Arian Karimi Rouzbahani, Zahra Haghighatian,* Yavuz Nuri Ertas,* and Bahareh Farasati Far*

Cite This: *ACS Appl. Mater. Interfaces* 2026, 18, 47237−47256

Read Online

ACCESS | Metrics & More | Article Recommendations | Supporting Information

ABSTRACT: Stimuli-responsive chitosan-based nanogels have attracted significant interest for drug delivery; however, many reported systems rely on synthetic crosslinkers and function primarily as passive carriers with limited control over network architecture and molecular transport. Here, we report a boswellic-acid-integrated, pH-responsive hybrid nanogel platform in which boswellic acid serves as a bioactive network modifier and hydrophobic domain-forming component within chitosan matrices. Chitosan-boswellic acid (CS-g-BOS) hydrogel precursors were first formed via formaldehyde-assisted network formation and subsequently converted into CS-g-BOS nanogels via STPP-mediated ionic condensation, yielding a shear-thinning porous hydrogel precursor and pH-responsive nanogels relevant to injectable formulation development. The triterpenoid constituents of BOS contribute to the formation of a heterogeneous network, introducing hydrophobic domains that regulate mesh size and diffusion pathways. Comprehensive physicochemical characterization (^{1}H NMR, FTIR, SEM, AFM, DLS, zeta potential, thermal stability, and rheological analyses) showed that BOS incorporation altered nanogel morphology, swelling behavior, rheological response, and release kinetics. The nanogels exhibited high sunitinib encapsulation efficiency (95.52%) and sustained, pH-dependent drug release over 18 days, with accelerated release under acidic tumor-mimicking conditions. Among the tested kinetic models, the Korsmeyer–Peppas model provided the best fit, suggesting that sunitinib malate (SUN) release is diffusion-dominated and modulated by pH-dependent swelling of the CS-g-BOS network. In vitro studies demonstrated cytotoxic and apoptosis-inducing activity against A549 human lung cancer cells, while hemolysis assays indicated favorable blood compatibility. Mouse xenograft studies showed tumor growth suppression, and the chick CAM assay demonstrated antiangiogenic activity; however, histological alterations in the liver, lungs, and kidneys indicated that systemic safety requires further optimization. Overall, this work presents a bio-derived hybrid-network strategy that integrates nanogel network engineering, transport control, and therapeutic functionality, offering a scalable alternative to conventional chitosan nanogels for tumor-responsive drug delivery applications.



KEYWORDS: *chitosan, nanogel, boswellic acid, lung cancer, sunitinib, pH-responsive release*

1. INTRODUCTION

Stimuli-responsive soft materials that dynamically regulate molecular transport across biological interfaces have become central to the design of advanced drug delivery systems. Among these materials, polymeric nanogels occupy a unique position because of their hydrated three-dimensional networks, high loading capacities, and tunable responses to environmental cues such as pH, temperature, and ionic strength.[1,2] The ability to precisely control network architecture at the nanoscale enables nanogels to bridge material structure with interfacial transport phenomena, making them attractive candidates for sustained, site-specific therapeutic delivery. Chitosan (CS)-based nanogels have been widely investigated because CS is biocompatible, biodegradable, and chemically versatile.[3] The amino and hydroxyl groups of CS enable facile chemical modification and ionic crosslinking, yielding nanogels with responsive swelling and controlled release under physiological conditions. Consequently, many CS nanogels have been developed for sustained and stimuli-responsive drug delivery applications.[4−6] However, many reported CS nanogels rely on

Received: February 9, 2026
Revised: July 1, 2026
Accepted: July 9, 2026
Published: July 20, 2026



ACS Publications

© 2026 American Chemical Society

crosslinking components that primarily serve structural roles, producing passive drug reservoirs with limited intrinsic biological functionality and poor control over release behavior. Moreover, decoupling crosslinking chemistry from biological activity restricts the establishment of clear structure–property–function relationships governing mesh size, diffusion pathways, transport kinetics, and interfacial interactions.[7] These limitations highlight the need for next-generation CS nanogels that integrate bio-derived structural components, pH-responsive behavior, and therapeutic functionality within a single, rationally engineered material platform. Despite extensive development, few CS nanogel systems have systematically linked crosslinker chemistry to network architecture (effective mesh size), transport kinetics, and interfacial delivery performance. Because nanogels are nanoscale hydrogel networks, the chemistry of bulk hydrogel precursor formation remains directly relevant to nanoscale swelling, mesh size, and release behavior. Accordingly, precursor hydrogel chemistry can govern the final nanogel swelling and release behavior. Hydrogels are three-dimensionally crosslinked hydrophilic polymer networks that can absorb large amounts of water and physiological fluids. Polysaccharides such as chitosan, alginate, pectin, and cellulose are commonly employed for hydrogel fabrication because of their abundance, chemical functionality, and favorable biocompatibility and biodegradability profiles.[8] Among natural polymers, CS has played a particularly important role in the development of drug delivery systems owing to its biocompatibility, biodegradability, low toxicity, and polyelectrolyte nature.[9] As a delivery matrix, CS facilitates chelation and adsorption processes and contains numerous hydroxyl and amine groups that respond sensitively to environmental pH variations. Recent advances in nanotechnology have further enabled the development of CS-based nanogels with customizable physicochemical properties for targeted cancer therapy. Omrani et al. demonstrated that combinations of covalent and noncovalent interactions can generate distinct CS nanogels that exhibit pronounced swelling under acidic conditions characteristic of tumor microenvironments.[10] Similarly, Farasati Far et al. reported sustainable synthesis strategies for highly swellable CS-based hydrogels and investigated their controlled drug-release behavior and cellular toxicity profiles, providing useful guidance for the design of hydrogel precursors. In particular, the interaction between CS and polyol phosphate salts, such as sodium tripolyphosphate (STPP), has been shown to yield pH-sensitive crosslinked networks, underscoring the importance of crosslinking chemistry in dictating the performance of hydrogel precursors and nanogels.[11]

In parallel with advances in polymeric materials, increasing attention has been directed toward the use of natural bioactive compounds for the prevention and treatment of chronic diseases, as these compounds often exhibit favorable safety profiles and multifunctional biological activity. The boswellic-acid-rich fraction used in this study, hereafter referred to as BOS, contains pentacyclic triterpenoids derived from *Boswellia serrata* resin, a natural source of compounds with reported anti-inflammatory, antidiabetic, anti-asthmatic, and anticancer properties. These biological effects arise from interactions of BOS with transcription factors, cell-surface receptors, and growth-factor signaling pathways.[12] From a materials perspective, the rigid triterpenoid backbones and multifunctional groups present in BOS suggest its potential to participate in hybrid network formation and introduce hydrophobic domains that may influence swelling and drug-release behavior. Previous studies have reported that specific boswellic acid derivatives, such as 11-carbonyl-β-boswellic acid, activate stress-related signaling pathways, induce PARP cleavage, suppress survivin expression, and inhibit proliferation in lung cancer cell lines.[13] Despite these promising biological properties, BOS has rarely been explored as a functional structural component within polymeric delivery networks, and its influence on the architecture of hydrogel precursors and the transport behavior of the resulting nanogels remains insufficiently understood.

Sunitinib malate (SUN) is a multitargeted tyrosine kinase inhibitor with well-established antitumor and antiangiogenic activity.[14] It has demonstrated efficacy against a variety of solid tumors, including breast, colorectal, neuroendocrine, and lung cancers, with reported clinical activity in non-small-cell lung cancer (NSCLC).[15] Although the pharmacokinetics of SUN have been extensively characterized, its therapeutic application remains limited by poor aqueous solubility, off-target toxicity, and difficulty maintaining sustained drug exposure at the tumor site. Accordingly, material-based delivery systems that improve local bioavailability, prolong release, and reduce systemic toxicity are of significant interest for enhancing SUN-based cancer therapy.[16,17]

In this study, we report a bio-derived, pH-responsive nanogel system in which BOS serves as a bioactive network modifier and hydrophobic domain-forming component within a CS-based network. Chitosan–BOS (CS-g-BOS) hydrogel precursors were prepared via formaldehyde-assisted network formation and subsequently converted into nanogels via STPP-mediated ionic condensation, yielding pH-responsive nanostructures derived from a stable porous precursor network. The precursor also exhibited shear-thinning rheology relevant to injectable formulation development. For clarity, CS-g-BOS hydrogel precursor refers to the bulk network obtained after formaldehyde-assisted CS-g-BOS network formation and gelation, whereas CS-g-BOS nanogels and SUN@CS-g-BOS nanogels refer to the nanoscale particles obtained after STPP-mediated ionic condensation in the absence or presence of SUN, respectively. SUN is used as a model anticancer agent to investigate drug-loading efficiency, transport regulation, and pH-dependent release behavior. Through comprehensive physicochemical characterization, transport analysis, and biological validation, we examine how incorporation of a bio-derived network modifier alters nanogel architecture, diffusion pathways, and release kinetics, while also contributing to therapeutic activity. This work demonstrates an integrated materials design strategy that couples bioderived network modification with controlled transport and anticancer activity, offering a scalable, biologically synergistic alternative to conventional CS nanogel systems.

2. EXPERIMENTAL

2.1. Chemicals and Materials

Medium-molecular-weight CS (MW ≈ 200,000 Da; degree of deacetylation, 98%), glacial acetic acid, sodium hydroxide, 37 wt % aqueous formaldehyde, 25 wt % aqueous ammonia, 37 wt % hydrochloric acid, and ethanol were obtained from Merck (Germany). *Boswellia serrata* oleo-gum resin was purchased from a local market, and SUN was kindly provided by Arasto Pharmaceutical Chemicals Inc., Tehran, Iran.

2.2. Extraction and Purification of a Boswellic-Acid-Rich Fraction

The oleo-gum resin of *Boswellia serrata* (30 mesh and oven-dried to 2% residual moisture content) was first cleaned to remove visible

https://doi.org/10.1021/acsami.6c02925
ACS Appl. Mater. Interfaces 2026, 18, 47237−47256

impurities and then defatted with *n*-hexane to remove waxy and other lipophilic components. A 50 g batch was packed into a 500 mL Soxhlet thimble and defatted with *n*-hexane (1:10 w/v) for 6 h. The dried marc (38 g) was transferred to a fresh Soxhlet apparatus and exhaustively extracted with 95% ethanol under gentle reflux at 70 °C. Three consecutive 8-h cycles with solvent replenishment, using a total solvent volume of 1.2 L, yielded an ethanolic extract. Ethanol was removed under reduced pressure (40 °C and 120 mbar) to 30% of the initial volume. The concentrate was diluted 1:1 with deionized water at 60 °C, then adjusted to pH 9.4 with 1 M NaOH, converting the boswellic acids into their water-soluble sodium salts. The resulting boswellic-acid-rich fraction is referred to as BOS throughout this manuscript. After 30 min of gentle stirring, the solution was cooled to 10 °C and acidified to pH 2.5 with 2 M HCl. Crude BOS precipitated as an off-white solid (yield 18–20% w/w of starting resin), in agreement with the Shah and Thomas patent, which emphasizes the pH-swing salting-out step as critical for selectivity.[18] The moist cake was washed to neutrality with chilled distilled water, then dried at 45 °C under 30 mmHg for 12 h to afford 8–10 g of BOS concentrate (65% purity by HPLC). For purification, 1 g portions were adsorbed on silica gel (60–120 mesh) and chromatographed on a 3 cm × 60 cm glass column. Elution began with *n*-hexane (100 mL) followed by stepwise gradients of hexane/ethyl acetate (9:1 to 7:3; v/v, total 600 mL). Fractions that exhibited an R_f value of 0.35 by TLC (toluene: EtOAc:AcOH 7:3:0.1) were pooled and recrystallized from ethyl acetate, yielding a purified BOS-rich fraction (≥90% by HPLC). This silica-based cleanup followed the workflow detailed by Fahim et al. and the WO 2014195976 protocol.[18,19] The identity and purity of each lot were confirmed using a Kinetex C18 (100 × 3 mm and 2.6 μm) column with a water/acetonitrile gradient containing 0.1% formic acid. Detection at 210 nm (quantification) and 254 nm (identity) separated α-BOS, β-BOS, KBOS, AKBOS, and their acetylated analogs within 10 min. FTIR fingerprinting showed characteristic C═O and O–H bands at 1705 and 3440 cm^{-1}, respectively.

2.3. Synthesis

A bulk CS-g-BOS hydrogel precursor was first synthesized; nanoscale CS-g-BOS and SUN@CS-g-BOS nanogels were then obtained from this precursor by STPP-mediated ionic condensation.[11] Briefly, CS (1200 mg) was dissolved in 1% (v/v) acetic acid and magnetically stirred for 8 h to obtain a homogeneous CS solution. Next, 37 wt % aqueous formaldehyde solution (5 mL) was added, and the mixture was allowed to react with amine groups under acidic conditions for 2 h, forming iminium intermediates (Figure 1). To promote CS-g-BOS network formation, 500 mg of BOS was introduced into the CS solution. The resulting mixture was then magnetically stirred for an additional 72 h. A 25 wt % aqueous ammonia solution (5 mL) was added to induce gelation, resulting in rapid formation of the CS-g-BOS hydrogel precursor. The hydrogel precursor was washed repeatedly with ethanol and methanol to remove unbound or unreacted species, including residual formaldehyde, and then filtered under vacuum. The absence of a distinct aldehyde band in the FTIR spectra was consistent with the removal of residual aldehyde, and the low hemolysis further supported the blood compatibility of the final nanogel formulation.

2.4. Characterization of Hydrogel Precursors and Nanogels

^{1}H NMR spectra were measured on a Bruker Avance DRX-500 spectrometer. Signal multiplicities are reported as singlet (s), doublet (d), triplet (t), quartet (q), and multiplet (m). Deuterium oxide (D_2O) was used as the solvent, and the residual HOD signal was used for internal calibration (δ_H = 4.79 ppm). Fourier transform infrared (FTIR) spectra were obtained in transmission mode on an Agilent Cary 630 (Agilent Technologies, USA) FTIR spectrometer without further sample preparation. Field-emission scanning electron microscopy (FESEM; Topcon, Singapore) was used to study the surface morphologies of freeze-dried CS-g-BOS hydrogel precursors and dried nanogels. The samples were coated with a 16-nm-thick gold film (Bal-tec, USA). Atomic force microscopy (AFM) was conducted in contact mode using a NanoScope E (Digital Instruments, USA). Hydrodynamic size, size distribution, and zeta potential were measured by dynamic and electrophoretic light scattering using a Zetasizer instrument (Nano ZS, Malvern Instruments, UK). Thermogravimetric analysis (TGA) was performed using an STA 449 F3 thermal analyzer (Netzsch, Germany). Measurements were conducted under a nitrogen atmosphere from 25 to 600 °C at 10 °C min^{-1}.

2.5. Swelling Behavior of the CS-g-BOS Hydrogel Precursors

To assess the swelling ratio, preweighed ball-milled CS-g-BOS hydrogel precursor powders were used. Each sample was immersed in media simulating gastric fluid (pH 1.2), intestinal fluid (pH 6.8), physiological/blood pH (pH 7.4), and acidic tumor conditions (pH 5.0), and then weighed at predetermined intervals. Additionally, the influence of varying temperatures (5, 25, 40, and 55 °C) on the swelling behavior of the hydrogel precursors was investigated. The swelling ratio and equilibrium water content of the hydrogel precursors were determined using the following equations:

$$\text{Swelling ratio } (SR) = (W_s - W_d)/W_d \quad (1)$$

$$\text{Equilibrium water content } (EWC\%) = (W_s - W_d)/W_s \times 100 \quad (2)$$

where W_d and W_s represent the dry and swollen hydrogel precursor masses, respectively.

2.6. Entrapment Efficiency Evaluation

CS-g-BOS hydrogel precursor powder (10 mg) was dispersed in 5 mL of deionized water, and SUN was added at carrier-to-drug ratios of 2:1 and 1:1, corresponding to 10 mg of carrier with 5 or 10 mg of SUN, respectively. The mixtures were stirred for 24 h in the dark at room temperature. Subsequently, 1 mL of a 2% (w/v) aqueous sodium tripolyphosphate (STPP) solution, equivalent to 20 mg of STPP, was added, giving a CS-g-BOS:STPP mass ratio of 1:2 (10 and 20 mg, respectively; w/w). The precursor powder was used as the starting material for nanogel formation. The resulting nanogels were collected by centrifugation at 10,000 rpm for 30 min and then dried. EE values were calculated separately for the 2:1 and 1:1 carrier-to-drug formulations, and the formulation with the higher EE was selected for subsequent release and biological experiments. The concentration of unencapsulated SUN was measured using a UV–vis spectrophotometer at a wavelength of 425 nm by analyzing the residual SUN in the supernatant. A standard curve for SUN was established by measuring absorbance at known concentrations to accurately quantify the drug in the supernatant. The entrapment efficiency (EE) was then determined using the following formula:

$$\textit{Entrapment efficiency}\ \text{efficiency (EE)}(\%) = \frac{(\text{Initial amount of SUN}) - (\text{Free amount of SUN})}{\text{Initial amount of SUN}} \times 100 \quad (3)$$

2.7. Drug Release Studies

SUN release was studied by dispersing dry SUN@CS-g-BOS nanogel powder in 50 mL of phosphate-buffered saline (PBS; pH 5.0 or 7.4) and maintaining the dispersion at 37 °C under mild stirring. At predetermined intervals, 3 mL of release medium was withdrawn and replaced with an equivalent volume of fresh medium. SUN quantification in PBS was performed using a spectrophotometer at 425 nm. The release study was continued for 18 days, during which the amount of drug released at each time interval was measured using calibration plots. The cumulative drug release was determined using the following

https://doi.org/10.1021/acsami.6c02925
ACS Appl. Mater. Interfaces 2026, 18, 47237−47256

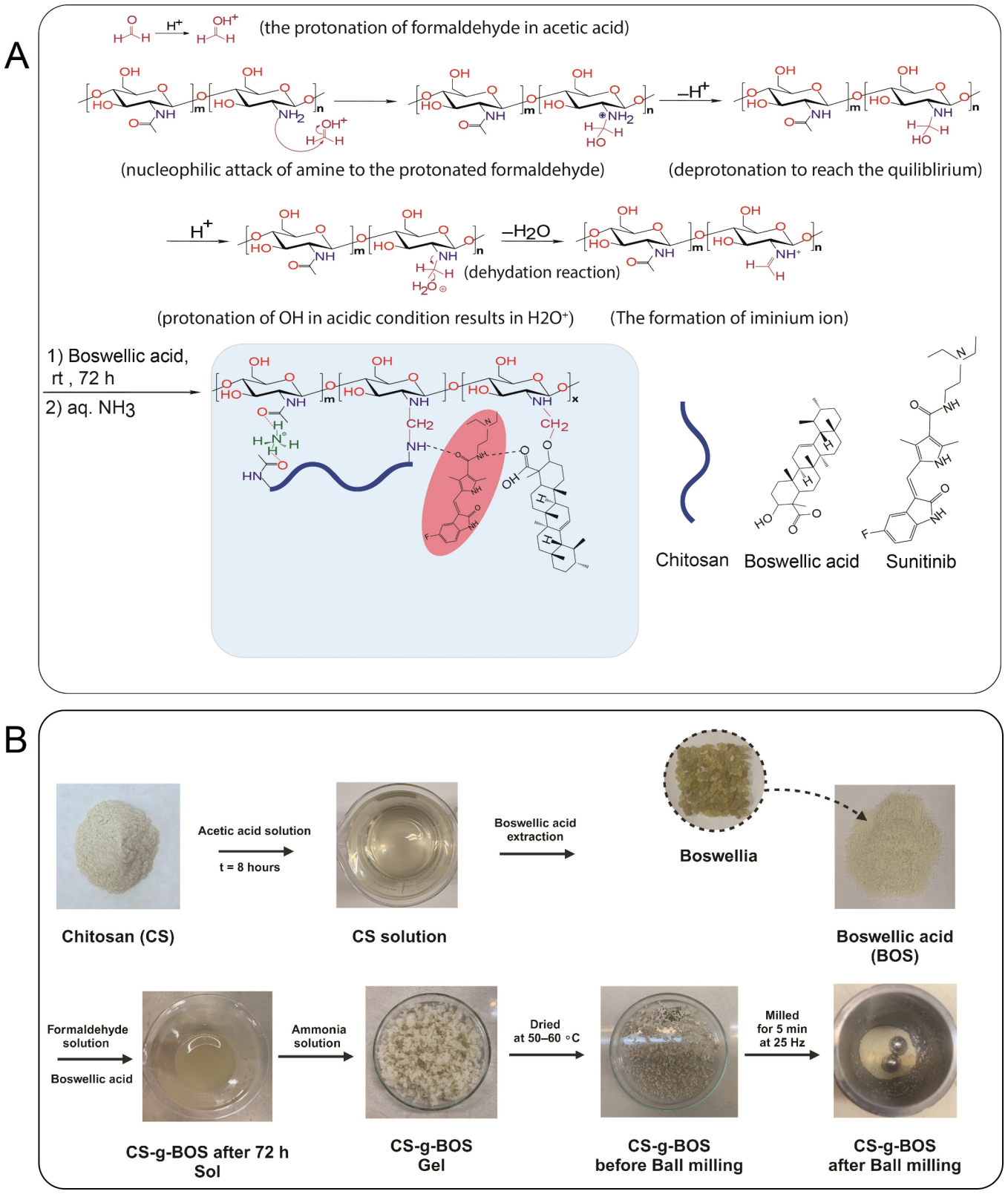


Figure 1. (A) Schematic illustration of formaldehyde-assisted network stabilization and noncovalent interactions, including ionic interactions, hydrogen bonding, and hydrophobic association with SUN. (B) Photographs showing the synthesis pathway of CS-g-BOS hydrogel precursor networks.

https://doi.org/10.1021/acsami.6c02925
ACS Appl. Mater. Interfaces 2026, 18, 47237−47256

equation:

$$Q = \frac{C_n \times V_0 + V_i \sum_{i=1}^{n-1} C_i}{m} \times 100\% \quad (4)$$

where Q represents cumulative drug release (%), C_n denotes the mass concentration of released drug, V_0 indicates the total volume of PBS, V_i refers to the sampling volume withdrawn at each interval, C_i is the drug concentration in the withdrawn sample at each time point, and m represents the mass of loaded SUN.

2.8. MTT Assay

The MTT (3-(4,5-dimethylthiazol-2-yl)-2,5-diphenyltetrazolium bromide) assay was used to determine the cytotoxic effects of conditioned media from CS-g-BOS and SUN@CS-g-BOS formulations on A549 and NIH3T3 cells. Cells were cultured in Dulbecco's Modified Eagle Medium (DMEM) supplemented with 10% fetal bovine serum (FBS), 100 U/mL penicillin, and 100 μg/mL streptomycin at 37 °C in a humidified atmosphere with 5% CO_2. Cells reached 70–80% confluence before the experiments were performed. Conditioned media were prepared by incubating unloaded CS-g-BOS or SUN@CS-g-BOS formulations at different concentrations in culture medium. Cells were seeded at 5000 cells per well in 96-well plates and allowed to attach overnight. Cells were treated with conditioned media collected from unloaded CS-g-BOS or SUN@CS-g-BOS nanogels at the indicated formulation concentrations; control wells received fresh culture medium alone. Thus, this assay evaluated the cytotoxicity of nanogel-released components rather than direct nanogel–cell interaction. Cells were incubated for 24 or 48 h. After treatment, MTT solution (5 mg/mL in PBS) was added to each well, and the plate was incubated for 4 h at 37 °C. Absorbance was measured at 570 nm using a microplate reader. Cell viability was calculated using the following formula, with control wells containing fresh culture medium without nanogel-conditioned medium set to 100% viability.

$$\text{Cell viability } (\%) = \frac{\text{Absorbance of treated cells}}{\text{Absorbance of control cells}} \times 100 \quad (5)$$

2.9. Fluorescence Microscopy Analysis of Apoptotic Cells

Triple fluorescence staining with DAPI, Annexin V-FITC, and PI was used to assess apoptosis. A549 cells were treated with fresh medium (control), free SUN, or SUN@CS-g-BOS conditioned medium for 48 h. The cells were then rinsed twice with 0.01 M PBS and resuspended in 200 μL of binding buffer. They were incubated with 10 μL of DAPI, 10 μL of Annexin V-FITC, and 5 μL of PI for 30 min at 4 °C in the dark. DAPI, Annexin V-FITC, and PI fluorescence signals were immediately examined using a confocal laser scanning microscope (Olympus, FV1000, Tokyo, Japan).

2.10. Flow Cytometry Analysis for Apoptosis Detection

A549 cells were seeded at a density of 5×10^5 cells per well in cell culture plates and incubated overnight at 37 °C in a 5% CO_2 atmosphere to ensure complete attachment. Subsequently, the cells were treated with CS-g-BOS, SUN, and SUN@CS-g-BOS at their respective IC_{50} concentrations for 24 h. Following treatment, the cells were harvested and washed twice with cold sterile PBS (pH 7.4). The cell pellets were resuspended in 1× binding buffer supplied with the apoptosis detection kit (Transgene Biotech ER101-01). Propidium iodide and Annexin V-FITC were added, and the cells were incubated for 10 min at ambient temperature. Finally, the cell suspensions were transferred to flow cytometry tubes and analyzed using a FACSCalibur flow cytometer (BD Biosciences, Franklin Lakes, NJ, USA).

2.11. Apoptosis-Related Gene Expression Analysis by RT-qPCR

A549 cells were treated with CS-g-BOS and SUN@CS-g-BOS at the corresponding IC_{50} concentrations for 24 h. Total RNA was extracted from treated and control cells using an RNA extraction kit according to the manufacturer's instructions. Complementary DNA (cDNA) was synthesized using a cDNA synthesis kit (Takara, Japan). Quantitative real-time PCR was performed using SYBR Green Master Mix (Bio-Rad, USA) on an iQ real-time PCR detection system. The apoptosis-related target genes were BAX, CDKN2A, CASP8, and CASP9, and B2M was used as the internal reference gene for normalization. The amplification protocol consisted of an initial denaturation at 95 °C for 10 min, followed by 35 amplification cycles according to the primer-specific conditions listed in Table S1. Relative gene expression was calculated from Ct values using the comparative $2^{-\Delta\Delta Ct}$ method after normalization to B2M. Electrophoresis on a 2% agarose gel was performed only to verify the expected amplicon size and PCR-product specificity; it was not used for quantitative expression analysis. Primer sequences are listed in Table S1.

2.12. Scratch Assay

The effects of control medium, CS-g-BOS hydrogel precursor specimens, free SUN, and SUN@CS-g-BOS hydrogel precursor specimens on 3T3 fibroblast migration were evaluated using a scratch assay. 3T3 cells were seeded at 5×10^4 cells/mL in 12-well plates and cultured overnight. After the cells reached 90% confluence, a linear scratch was created using a 100 μL pipette tip. Cell debris was removed by aspiration. Subsequently, CS-g-BOS and SUN@CS-g-BOS hydrogel precursor specimens, each weighing approximately 10 mg and measuring 8 mm in diameter, were placed in wells containing 3T3 fibroblast cultures; free SUN was added to the designated treatment wells, and all groups were incubated for 24 h at 37 °C in a humidified atmosphere containing 5% CO_2. After 24 h, 3T3 fibroblast migration was documented using an Olympus X53 microscope. The migration distance was subsequently determined using ImageJ software, as previously described.[20] The experiment was performed in triplicate, and results are reported as mean ± SD.

2.13. Hemolysis Assay

Hemolytic activity was assessed as previously described.[21] Fresh human blood was collected into EDTA tubes. The blood was centrifuged for 10 min at 10,000 rpm to pellet erythrocytes, and the supernatant was removed. CS-g-BOS nanogel formulations were added to the blood samples at final concentrations of 200, 400, 600, 800, and 1000 μg/mL, and the final volume was adjusted to 1 mL with PBS. The resulting samples were then incubated in a shaking incubator for 4 h at 80 rpm. After incubation, samples were centrifuged for 10 min at 5000 rpm. The absorbance of the supernatant was measured at 540 nm in triplicate using a Rayto RT-6000 spectrophotometer. Triton X-100 was used as the positive control, whereas blood samples in PBS served as negative controls. Hemolytic activity (%) was calculated using eq (6).

$$\text{Hemolysis } (\%) = \frac{\text{Absorbance of sample–Absorbance of Negative Control}}{\text{Absorbance of Positive Control–Absorbance of Negative Control}} \times 100 \quad (6)$$

2.14. Histopathology Analysis

The lung, heart, liver, kidney, spleen, and tumor specimens were dehydrated, cleared, and paraffin-embedded overnight using an automatic tissue processor (Sakura, Japan). The samples were embedded in paraffin using an embedding apparatus (Sakura, Japan), and consecutive 4 μm sections were cut using a microtome (Model RM2245, Leica Biosystems, Wetzlar, Germany). An autostainer (Model 5020, Leica Biosystems, Wetzlar, Germany) was used for hematoxylin and eosin

https://doi.org/10.1021/acsami.6c02925
ACS Appl. Mater. Interfaces 2026, 18, 47237–47256

(H&E) staining. The mounted specimens were examined under light microscopy.

2.15. In Vivo Investigation

A total of 20 female BALB/c nude mice, weighing 18 ± 2 g and aged 6–8 weeks, were randomly allocated to four groups (n = 5 per group). Mice were maintained at a stable temperature of 23 ± 2 °C, a relative humidity of 55%, and a 12-h light/dark cycle. A549 cells were used to establish subcutaneous lung adenocarcinoma xenografts. Briefly, after cell counting, a suspension containing 2×10^6 cells was prepared in sterile 1× PBS and then injected subcutaneously into the right flank of the mice. Tumor volume was measured using a digital caliper. When tumors reached approximately 80 mm^3, mice were assigned to control, CS-g-BOS, SUN, and SUN@CS-g-BOS groups. Formulations were administered by intravenous tail-vein injection on days 1, 5, and 10. Body weight was measured at 2-day intervals during the treatment phase. SUN and SUN@CS-g-BOS were administered at a SUN-equivalent dose of 10 mg/kg in 100 μL per injection; the CS-g-BOS group received an equivalent carrier dose, and the control group received the corresponding vehicle. Mice were euthanized after 11 days of treatment. The tumors were then excised immediately and stored in 10% formalin. Tumor volume was calculated using the following formula:

$$\text{Volume} = 1/2 \times (\text{Width}^2) \times \text{Length} \quad (7)$$

2.16. Chick Chorioallantoic Membrane (CAM) Angiogenesis Assay

The antiangiogenic activity of SUN@CS-g-BOS was evaluated using the CAM assay.[22] Three-day-old fertilized eggs were gently cleaned with lukewarm water, allowed to dry, and then sterilized by spraying with ethanol before being placed in the incubator at 37 °C with a relative humidity of 40–60%. After 5 days of incubation, a circular window approximately 1.5–2 cm in diameter was drilled in the eggshell to expose the CAM, taking care to remove any residual shell fragments. PBS was used as the control, CS-g-BOS was used as the blank carrier control, and SUN@CS-g-BOS formulations were applied to the chorioallantoic membrane of 8-day-old embryos at total formulation masses of 15 or 30 mg per CAM. The window was then sealed with tape, and the eggs were returned to the incubator. The CAM vasculature was photographed daily. On day 14, the eggs were opened, and images of blood vessels were captured using a digital camera at ×10 magnification. Angiogenesis was assessed from digitized images by quantifying the total length of blood vessels in ImageJ. Measurements were performed independently by three investigators in the regions surrounding the treatment site, covering approximately 50% of the CAM surface.

2.17. Statistical Analysis

GraphPad Prism version 8 was used for statistical analysis. Data are presented as mean ± standard deviation (SD) unless otherwise indicated. The number of experimental or biological replicates is provided in the corresponding figure legends. In vitro assays were performed at least three times with technical replicates as appropriate. For in vivo experiments, n = 5 animals per group. The number of eggs/embryos collected per group in CAM assays is shown in the figure legend. Normality and homogeneity of variance were assessed before parametric testing. Multiple comparisons among the groups were performed using one-way ANOVA with Tukey's post hoc test. A two-tailed Student's t-test was used to compare two groups as appropriate. $p < 0.05$ was considered statistically significant. Significance levels are indicated as $^*p < 0.05$, $^{**}p < 0.01$, $^{***}p < 0.001$, and $^{****}p < 0.0001$.

3. RESULTS AND DISCUSSION

3.1. Synthesis Mechanism of CS-g-BOS

CS hydrogel networks can form through physical or chemical interactions, depending on the application.[23,24] Figure 1A,B depict the CS-g-BOS hydrogel precursor design approach. The first step in the synthesis was the preparation of a CS solution, followed by protonation under acidic conditions. CS amine groups were protonated in acetic acid, generating positively charged ammonium groups. Following protonation, formaldehyde was added to the CS. Iminium intermediates, which are stabilized cations, formed when formaldehyde reacted with protonated amine groups. BOS-associated nucleophilic groups may have reacted with iminium intermediates on the CS backbone. This step may have promoted CS-g-BOS network formation by enabling interactions between iminium intermediates on the CS backbone and reactive functional groups associated with BOS. The mixture was allowed to form a mixed-interaction network at room temperature over 72 h. Finally, an ammonia solution was added to complete precursor gelation. The resulting product was a CS-g-BOS hybrid hydrogel precursor containing incorporated BOS molecules. Hydrogen bonding, electrostatic attraction, and hydrophobic interactions were likely important for precursor gelation.[10] The SUN-containing CS-g-BOS precursor mixture was treated with aqueous STPP to form SUN@CS-g-BOS nanogels. BOS incorporation into the CS-g-BOS network may have enhanced SUN loading efficiency. Interactions among CS, BOS, formaldehyde-derived linkages, and SUN may have contributed to drug retention (Figure 1B).

Figure 2 illustrates the CS-g-BOS hydrogel network, its interactions with SUN, and the subsequent STPP-mediated formation of SUN-loaded nanogels for drug release. Hydrogen bonding can occur between hydroxyl, amine, carboxyl, and carbonyl groups present in CS, BOS, and SUN. Electrostatic interactions can occur between protonated amine groups on CS and acidic/carboxylate groups associated with BOS, and possible imine/iminium-derived linkages and/or methylene-type bridges may contribute to network stabilization. The bulk CS-g-BOS hydrogel precursor network initially entraps SUN within its porous structure, and subsequent STPP-mediated ionic condensation forms SUN@CS-g-BOS nanogels. Hydrogen bonding between SUN and the polymeric network helps retain the drug within the nanogel-forming matrix. Hydrophobic association between BOS-rich domains and SUN may also promote SUN retention within the nanogel network. SUN release from the nanogel also depends on the mesh size relative to the molecular dimensions of SUN.[25] If the mesh size is significantly larger than the drug molecule, the drug can diffuse through the network more rapidly. If the mesh size is similar to the molecular dimensions of the drug, the drug moves through the network more slowly and in a controlled manner. As the nanogel swells, relaxes, or degrades, SUN is released and can diffuse into the surrounding medium or tissue. The schematic illustrates that BOS may help stabilize the hydrogel precursor and regulate drug release through physical entrapment, possible covalent linkages, and hydrophobic domain formation. Collectively, these interactions suggest the formation of a heterogeneous mixed-interaction network in which possible covalent stabilization, STPP-mediated ionic condensation, hydrogen bonding, and

https://doi.org/10.1021/acsami.6c02925
ACS Appl. Mater. Interfaces 2026, 18, 47237−47256

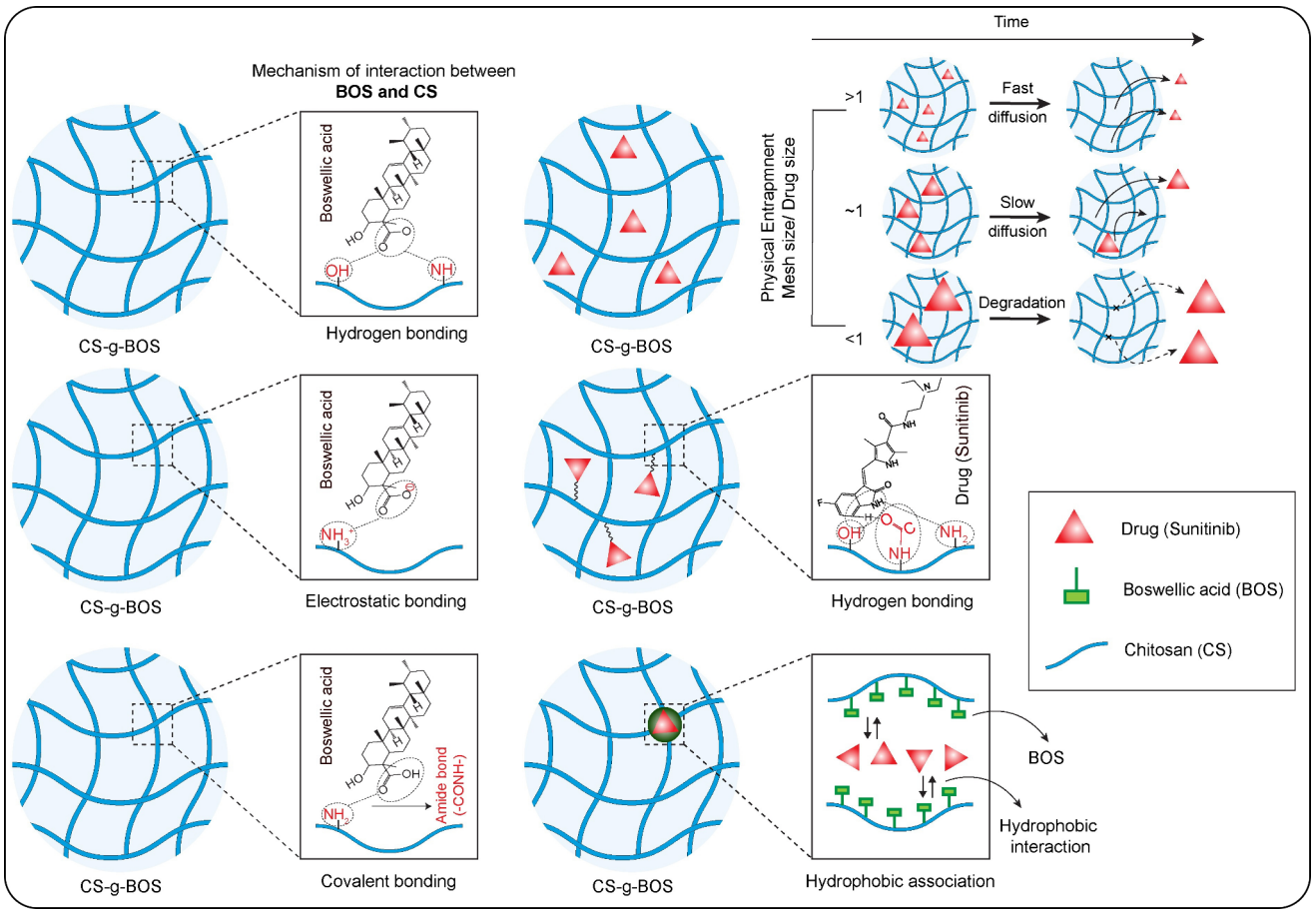


Figure 2. Schematic illustration of the mixed-interaction CS-g-BOS nanogel platform and proposed SUN-retention/release mechanisms. Formaldehyde-assisted network formation produces a CS-g-BOS hydrogel precursor network in which BOS may contribute through hydrogen bonding, electrostatic interactions, hydrophobic association, and possible iminium- or methylene-type covalent stabilization. During STPP-mediated ionic condensation, the precursor network is converted into SUN-loaded CS-g-BOS nanogels. SUN retention within the nanogel network is promoted by physical entrapment, hydrogen bonding, electrostatic interactions, and hydrophobic association between SUN and BOS-rich domains. The mesh size of the nanogel network relative to the molecular dimensions of SUN regulates diffusional transport, whereas pH-dependent swelling and possible network relaxation/degradation further modulate SUN release.

hydrophobic association collectively contribute to nanogel integrity, swelling behavior, and SUN retention.

3.2. Characterization of Hydrogel Precursors and Nanogels

3.2.1. ^{1}H NMR Analysis. The ^{1}H NMR spectrum of CS-g-BOS is shown in Figure 3A. The intense resonance at 4.7–4.9 ppm was attributed to residual HOD/water in D_2O. The signal around 3.71 ppm was assigned to the H1 and H3–H6 protons of CS, consistent with the characteristic CS proton signals observed between 3.4 and 4.0 ppm.[26] Signals at 1.96–2.30 ppm were assigned to acetyl methyl protons, whereas signals near 2.84–2.90 ppm corresponded to the H2 proton of CS.[27] A weak/broad resonance around 4.5 ppm may be associated with methylene-type environments generated during formaldehyde-assisted network formation (H8 and H9).[23] However, because this region overlaps with CS saccharide protons and solvent-related broadening, this signal cannot be used alone as definitive evidence of covalent CS-g-BOS grafting. The ^{1}H NMR data, therefore, support BOS incorporation into the CS-based network rather than providing quantitative proof of covalent substitution. Accordingly, the CS-g-BOS network was interpreted as a mixed-interaction structure, involving possible covalent stabilization, ionic interactions, hydrogen bonding, and hydrophobic association. The downfield feature near 4.9 ppm was consistent with hydrogen-bonding effects involving the anomeric proton (H1), whereas the signals around 1.5–2.2 ppm were assigned to BOS triterpenoid protons, including α-methine, oxymethine, alicyclic methine, alicyclic methylene, and angular tertiary methyl protons.

3.2.2. FTIR Analysis. The FTIR spectra of CS (a), BOS (b), SUN (c), CS-g-BOS (d), and SUN@CS-g-BOS (e) are shown in Figure 3B. CS showed bands at 1657 and 1587 cm^{-1}, assigned to the amide I and amide II vibrations, respectively.[28] The band at 1587 cm^{-1} corresponds to the N–H bending vibration, which overlaps the amide II vibration, and the band at 1657 cm^{-1} is the amide I vibration. Furthermore, the stretching vibrations of C–N occur between 1160 and 925 cm^{-1} and overlap with the vibrations of carbohydrate rings. The N–H stretching band overlaps with the O–H stretching band from the carbohydrate ring in the 3325–3225 cm^{-1} region. In the BOS spectrum, the broad band near 3472 cm^{-1} is assigned to O–H stretching, bands at ~2937 cm^{-1} to aliphatic C–H stretching, a strong band at

https://doi.org/10.1021/acsami.6c02925
ACS Appl. Mater. Interfaces 2026, 18, 47237−47256

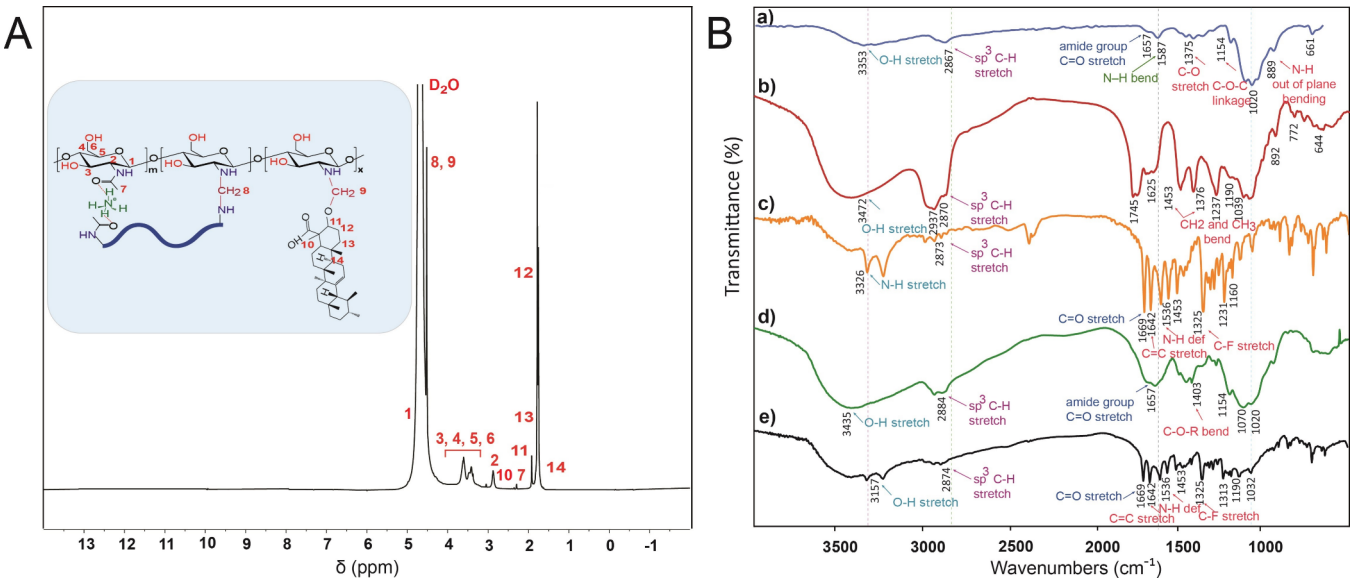


Figure 3. (A) ^{1}H NMR spectrum (500 MHz, D_2O, and 25 °C) of CS-g-BOS. (B) FTIR spectra of (a) CS, (b) BOS, (c) SUN, (d) CS-g-BOS, and (e) SUN@CS-g-BOS.

~1745 cm^{-1} to C═O stretching (carboxylic acid/ester), and bands near ~1625 cm^{-1} to C═C stretching. Additional fingerprint-region bands (1453–1039 cm^{-1}) arise from C–H bending and C–O stretching. SUN showed strong absorption bands at 3326 cm^{-1} (N–H stretching), 1231 cm^{-1} (aryl C═C/C–H vibrations), 2860-2890 cm^{-1} (C–H group, alkyl), 1669 cm^{-1} (–NH–C═O group), and 1325 cm^{-1} (C–F group). CS-g-BOS showed bands with reduced peak intensity compared with CS and BOS, supporting BOS incorporation into the CS-based network (Figure 3B).

These spectral changes support BOS incorporation into the CS-based network and indicate extensive intermolecular interactions. The broad band around 3435 cm^{-1} is consistent with enhanced hydrogen bonding between CS and BOS functional groups. Changes in the 1700–1400 cm^{-1} region may reflect overlapping contributions from BOS carbonyl/carboxyl groups, chitosan amide/amine vibrations, ionic interactions, and possible formaldehyde-assisted methylene/iminium-derived linkages. However, because these bands overlap substantially, FTIR alone cannot distinguish covalent CS-g-BOS coupling from strong physical association. The band near 1403 cm^{-1} may be associated with C–O–R/C–O vibrations in the BOS–CS network. The SUN-loaded CS-g-BOS spectrum showed similar bands with reduced intensity relative to CS-g-BOS, indicating that SUN was encapsulated in CS-g-BOS nanogels. Therefore, FTIR provides supportive evidence for the formation of a mixed-interaction network rather than definitive proof of covalent grafting. Comparison of CS-g-BOS and SUN@CS-g-BOS FTIR spectra revealed bands associated with C═C, C–F, and C–H vibrations, supporting successful SUN encapsulation.[29]

3.2.3. Morphological Analysis of CS-g-BOS Hydrogel Precursors and Nanogels. Figure 4A illustrates a porous, interconnected CS-g-BOS hydrogel precursor that is stabilized by hydrogen bonding and BOS-associated interaction domains, followed by STPP-mediated ionic condensation to form nanogels. Mixing the CS-g-BOS precursor dispersion with STPP facilitates ionic interactions and crosslinking, thereby forming nanogels. Additionally, SUN can be incorporated into the precursor dispersion during STPP-mediated ionic condensation, yielding SUN-loaded nanogels. Figure 4B,C show the morphologies of freeze-dried CS-g-BOS and SUN-loaded CS-g-BOS hydrogel precursors before STPP addition. FESEM images showed that these hydrogel precursors exhibited high porosity and a 3D interconnected porous structure. The formation of crosslinked networks may explain the interconnections between pores in CS-g-BOS hydrogel precursors. During freezing and drying, water removal leaves pores within the hydrogel precursor network, increasing apparent porosity. The porous architecture can facilitate swelling, water transport, and SUN entrapment. The CS-g-BOS hydrogel precursor exhibited a well-defined porous structure with a mean pore size of 40.49 μm, whereas the SUN-loaded CS-g-BOS hydrogel precursor showed an average pore size of 25.90 μm. This smaller mean pore size may be attributed to SUN entrapment within the porous structure. To examine the morphology of the hydrogel-derived nanogels after STPP addition, FESEM was used (Figure 4D,E). FESEM analysis of the nanogels was performed in the dry state under vacuum conditions. FESEM images of nanogels indicated that the particles were spherical or nearly spherical. According to the particle size distribution, STPP-mediated ionic condensation produced nanogels with a relatively uniform size distribution. The SUN@CS-g-BOS nanogels had an average particle size of 470.80 nm, whereas the CS-g-BOS nanogels showed an average particle size of 221.77 nm. AFM analysis revealed that the nanogels were spherical. CS-g-BOS nanogels were approximately 17 nm high and had a diameter of 60–300 nm (Figure 4F–I). The maximum height of SUN@CS-g-BOS nanogels was 26.2 nm, approximately 50% higher than that of unloaded CS-g-BOS nanogels. The increase was attributed to SUN incorporation into the nanogel matrix. A previous AFM study reported CS/TPP nanogel diameters ranging from 200 to 400 nm.[30]

3.2.4. Dynamic Light Scattering and Zeta Potential Analyses. The DLS data for CS-g-BOS nanogels indicated a relatively narrow size distribution (Figure S1A), with the

https://doi.org/10.1021/acsami.6c02925
ACS Appl. Mater. Interfaces 2026, 18, 47237−47256

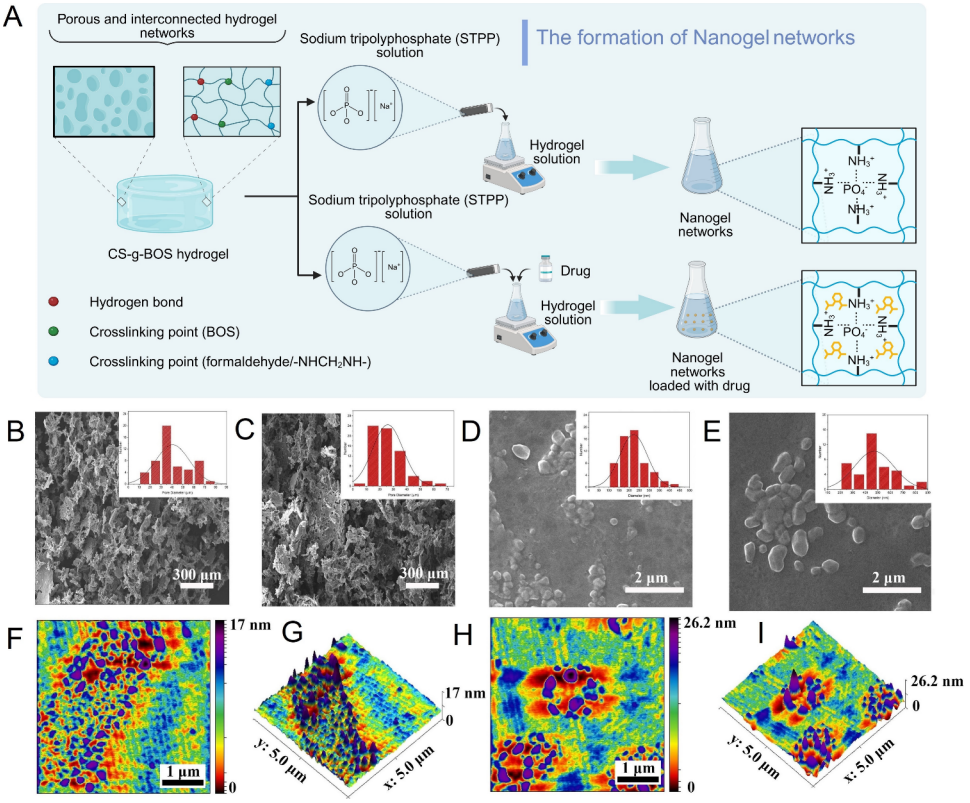


Figure 4. Morphological characterization of hydrogel precursors and nanogels. (A) Schematic of the CS-g-BOS hydrogel precursor formation and subsequent STPP-mediated nanogel formation. (B, C) FESEM images and pore-size distributions of the freeze-dried unloaded and SUN-loaded hydrogel precursors. (D, E) FESEM images and particle-size distributions of unloaded and SUN-loaded nanogels. (F, G) 2D and 3D AFM images of unloaded nanogels. (H, I) 2D/3D AFM images and root-mean-square roughness analysis of SUN-loaded nanogels.

majority of particles concentrated around 176.6 nm. SUN@CS-g-BOS nanogels exhibited a broader size distribution that was shifted toward larger particle sizes relative to that of the CS-g-BOS nanogels. This observation supports SUN incorporation into the nanogel network and the resulting increase in particle size (Figure S1B). The difference between FESEM- and DLS-derived particle sizes may be attributed to differences between dry-state imaging and hydrated-state light-scattering measurements, as well as partial particle agglomeration during sample preparation. Zeta potential reflects the surface charge of suspended particles and is commonly used to assess colloidal stability. Both CS-g-BOS and SUN@CS-g-BOS formulations exhibited more positive zeta potentials at pH 5.0 than at pH 7.4 (Figure S1C). An acidic environment increases electrostatic repulsion between nanogels by protonating functional groups, thereby improving dispersion and increasing colloidal stability. The increased zeta potential at acidic pH may enhance interactions with negatively charged cell membranes, thereby improving drug delivery and controlled drug release.[11] The nanogels exhibited pH-sensitive properties, enabling them to serve as effective pH-responsive delivery platforms.

3.2.5. Swelling Behavior. The swelling behavior of the CS-g-BOS hydrogel precursor at 5, 25, 40, and 55 °C is presented in Figure 5 The data indicated that increasing the temperature from 5 to 40 °C increased the swelling ratio of the CS-g-BOS hydrogel precursor. CS-g-BOS exhibited weakened hydrogen bonding at higher temperatures, facilitating water entry and leading to a more pronounced swelling response. Conversely, the hydrogel precursor exhibited stronger hydrogen bonding at lower temperatures, thereby inhibiting water penetration. When the temperature increased from 40 to 55 °C, the swelling of the CS-g-BOS hydrogel precursor decreased. This decrease may indicate reduced stability of the hydrogel precursor or partial degradation at 55 °C.[10] The swelling of the CS-g-BOS hydrogel precursor was attributed to hydrogen bonding between water molecules and hydrophilic amine ($-NH_2$) and hydroxyl (–OH) groups present in the CS and BOS chains. The CS-g-BOS hydrogel precursor exhibited a higher swelling ratio at pH 5.0, mimicking acidic tumor conditions, than at pH 7.4, which represents physiological blood pH. Under acidic conditions, CS amine groups become protonated, forming positively charged $-NH_3^+$ groups. The resulting electrostatic repulsion among protonated amine groups expands the polymer network, reduces effective network compactness, and facilitates water uptake, thereby increasing swelling. In contrast, at pH 7.4, partial deprotonation of CS amine groups reduces electrostatic repulsion, allowing the network to adopt a more compact structure and resulting in lower swelling.[31−33]

3.2.6. Thermal Stability Analysis. The CS-g-BOS hydrogel precursor exhibited two weight-loss stages. Loss of physically adsorbed water accounted for an initial weight loss of 8.16% at 147 °C. Thermal decomposition of crosslinks within the hydrogel precursor network and the polysaccharide backbone resulted in approximately 89% mass loss of CS-g-BOS (132–600 °C) (Figure 5E). A previous study of CS-g-glycerol and carboxymethyl CS-g-glycerol hydrogels showed weight loss

https://doi.org/10.1021/acsami.6c02925
ACS Appl. Mater. Interfaces 2026, 18, 47237−47256

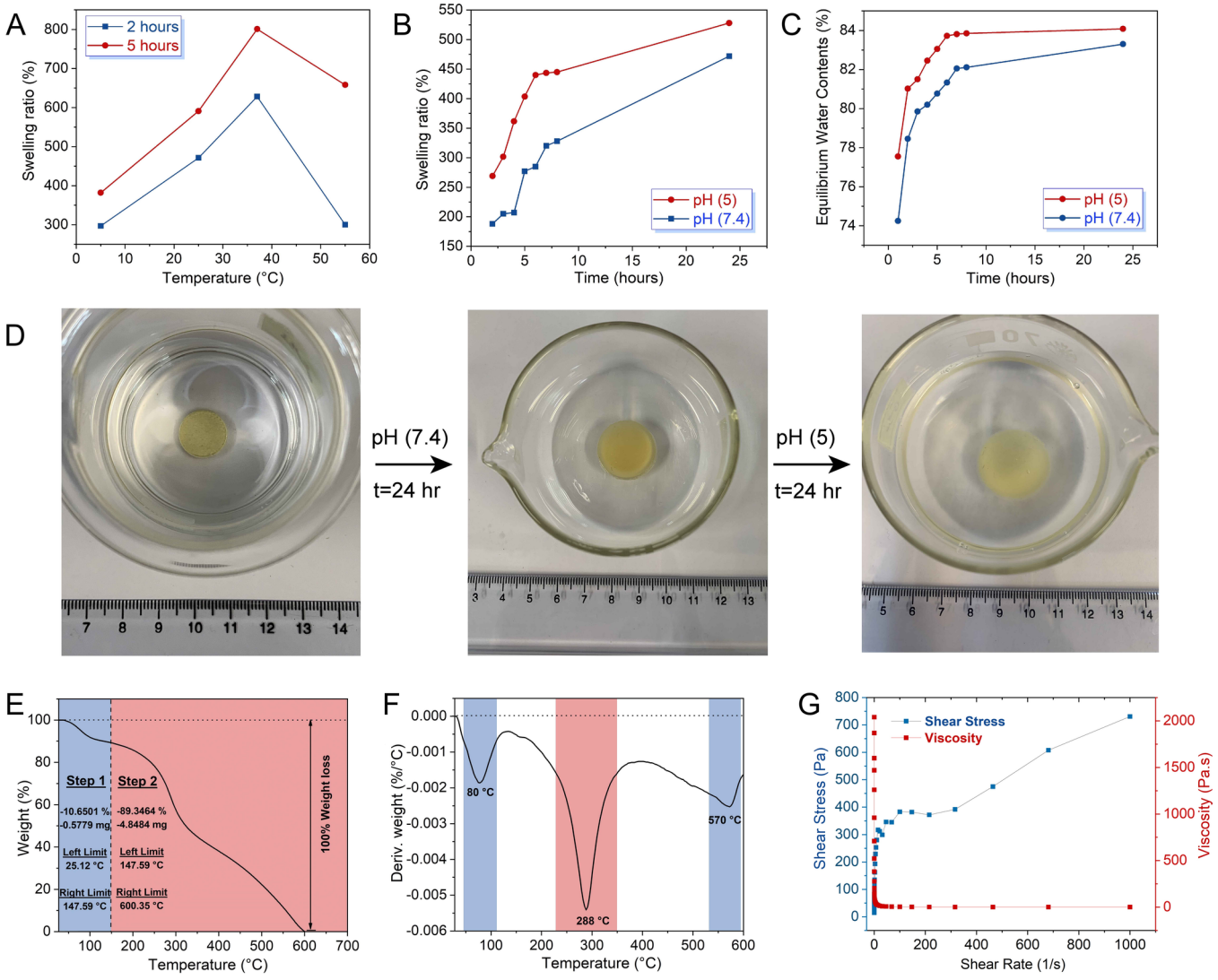


Figure 5. Physicochemical characterization of the CS-g-BOS hydrogel precursor. (A) Temperature-dependent swelling behavior at 5, 25, 40, and 55 °C after 2 and 5 h. (B) pH-dependent swelling behavior after 24 h. (C) Equilibrium water content after 24 h at pH 7.4 and 5.0. (D) Visual observation of pH-dependent swelling after 24 h. (E, F) TGA and DTG curves of the precursor. (G) Viscosity–flow curve of the precursor dispersion.

at 230–600 °C due to polymer structural degradation and the thermal breakdown of the pyranose ring of CS.[11] The CS-g-BOS hydrogel precursor was also analyzed by differential thermogravimetry (DTG) (Figure 5F). The DTG curve indicated that the CS-g-BOS hydrogel precursor degraded in two steps between 25 and 600 °C, with the main decomposition peak observed at 257 °C.

3.2.7. Rheological Properties. The CS-g-BOS hydrogel precursor dispersion exhibited shear-thinning behavior, with viscosity decreasing as shear rate increased (Figure 5G). At very low shear rates (<10 s^{-1}), the viscosity values were high (~2000 Pa·s), suggesting a stable and highly interconnected three-dimensional polymer network stabilized by intermolecular interactions and chain entanglements. A significant drop in viscosity was observed as the shear rate increased to 1000 s^{-1}, indicating progressive disruption of intermolecular interactions and the alignment of the polymer chains along the flow direction. Concurrently, the shear stress increased continuously from approximately 50 Pa at a low shear rate to about 730 Pa at 1000 s^{-1}, indicating the ability of the hydrogel precursor to withstand stress under applied shear. These findings agree with prior reports on CS-based hydrogels showing non-Newtonian, pseudoplastic behavior.[34,35] Studies on the rheological behavior of CS-graft-gelatin and acrylamide-sodium alginate dual network hydrogels have shown similar shear-thinning behavior, with the viscosity of the hydrogel decreasing with increasing shear rates.[36,37]

3.3. Hemolysis Assay

Hemolysis is a key indicator of blood compatibility and reflects red blood cell membrane disruption following exposure to the material (Figure 6A,B). Triton X-100 produced 97.36% hemolysis and served as the positive control.

CS-g-BOS nanogels exhibited 2.44% hemolysis at 1000 μg/mL, remaining below the commonly used 5% hemolysis threshold. Even at the highest tested concentration, CS-g-BOS nanogels showed minimal hemolytic activity against red blood cell (RBC) membranes (Figure 6C). The hydrophilic

https://doi.org/10.1021/acsami.6c02925
ACS Appl. Mater. Interfaces 2026, 18, 47237−47256

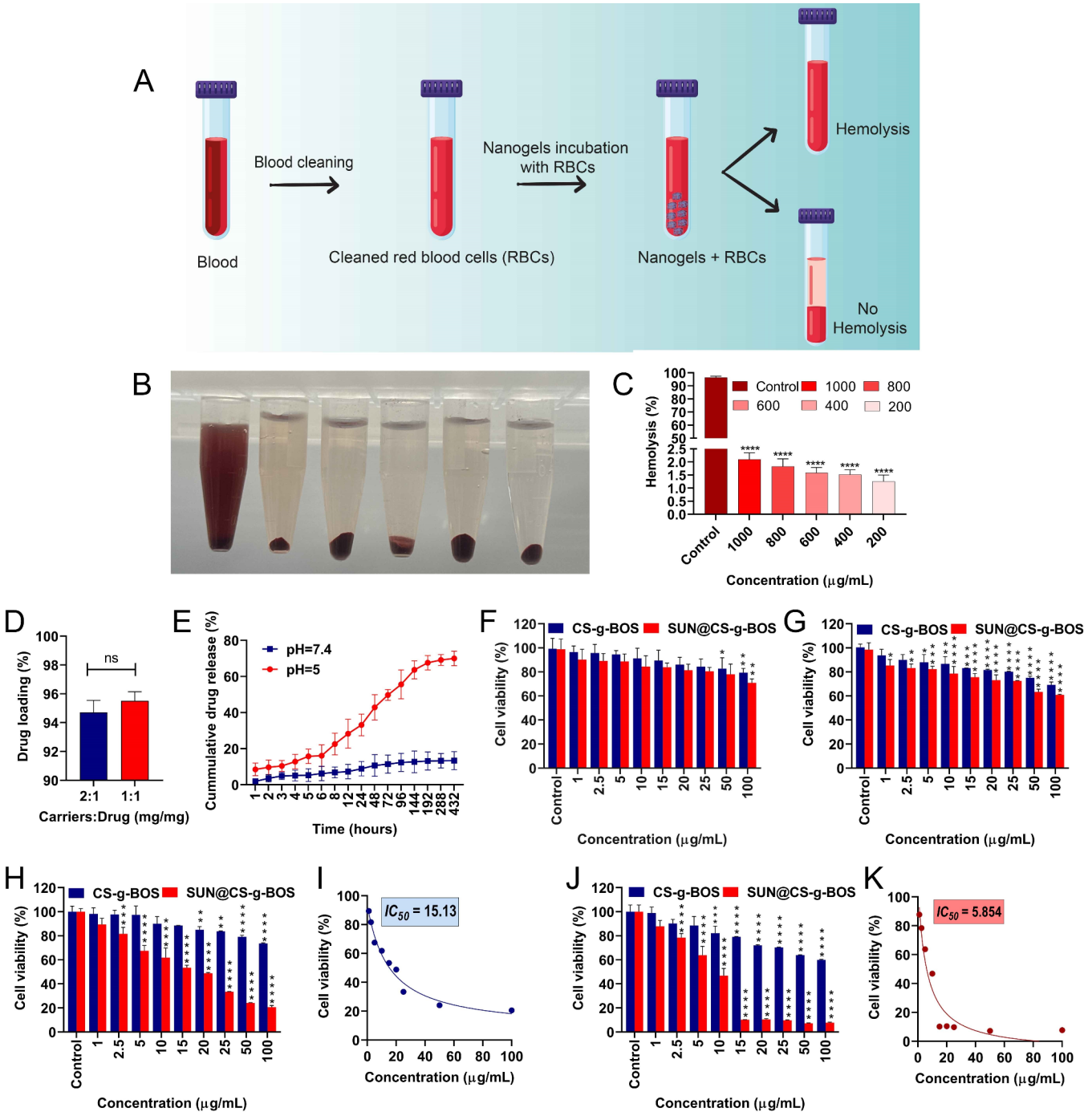


Figure 6. (A) Schematic illustration of the hemolysis assay after treatment with nanogels. (B) Visual observation of hemolysis at different nanogel concentrations. (C) Hemolysis assay results for CS-g-BOS. (D) Entrapment efficiency of SUN@CS-g-BOS prepared using 2:1 and 1:1 carrier-to-drug mass ratios (10:5 and 10:10 mg carrier:drug) and 2% STPP. (E) SUN release profile from SUN@CS-g-BOS in PBS at pH 7.4 and 5.0 at 37 °C over 432 h. (F, G) Cytotoxicity of conditioned media from CS-g-BOS and SUN@CS-g-BOS formulations toward NIH3T3 cells after 24 and 48 h. (H, J) Cytotoxicity of conditioned media from CS-g-BOS and SUN@CS-g-BOS formulations toward A549 cells after 24 and 48 h. (I, K) IC_{50} values calculated for conditioned media from SUN@CS-g-BOS nanogels against A549 cells after 24 and 48 h, respectively.

character and crosslinked network structure of CS-g-BOS nanogels may reduce lipid bilayer disruption. The low membrane disruption may also reflect weak interactions between the CS-g-BOS nanogel surface and RBC membranes at the tested concentrations. Although hemolysis increased slightly with concentration, it remained below the 5% threshold. The CS-g-BOS nanogel network structure, along with its surface charge, may influence the degree of hemolysis. Protonated amine groups may form electrostatic interactions with negatively charged RBC membranes and potentially contribute to phospholipid bilayer disruption. As the CS-g-BOS nanogel concentration increases, stronger surface-mediated interactions with RBC

https://doi.org/10.1021/acsami.6c02925
ACS Appl. Mater. Interfaces 2026, 18, 47237−47256

membranes may occur;[38] however, hemolysis remained below 5% under all tested conditions.

3.4. Drug Release and Kinetic Models

SUN@CS-g-BOS nanogels were prepared using 2:1 and 1:1 carrier-to-drug mass ratios (10:5 and 10:10 mg carrier:drug), resulting in entrapment efficiencies of 94.00% and 95.52%, respectively (Figure 6D). The 1:1 carrier-to-drug mass ratio, which showed the highest EE (95.52%), was selected as the optimal formulation for subsequent release and biological studies. Figure 6E illustrates the comparative release profiles of SUN in PBS at pH 5.0 and 7.4 at 37 °C. SUN release was pH-dependent. Release profiles were similar during the first 4 h, but acidic conditions accelerated release thereafter. This likely reflects similar early swelling in both media, which minimized differences in diffusion path length during the first 4 h.[33] During the initial 12 h, 28.33% of SUN was released from SUN@CS-g-BOS nanogels at pH 5.0, whereas 7.32% of SUN was released at pH 7.4. After 18 days, cumulative SUN release was 70.03% at pH 5.0 and 13.35% at pH 7.4. These results indicate that SUN release depends on both time and pH.

The kinetics of SUN release from the nanogels were evaluated using the Korsmeyer–Peppas, Higuchi, first-order, and zero-order models. Model fit was evaluated using the coefficient of determination (R^2) from the regression analysis. The rate constants and correlation coefficients for SUN release from SUN@CS-g-BOS nanogels at varying pH levels are presented in Figure S2. The zero- and first-order fits for SUN release from SUN@CS-g-BOS nanogels at pH 7.4 yielded R^2 values of 0.5692 and 0.5791, respectively, suggesting that these models are not suitable for describing the release kinetics. The Korsmeyer–Peppas model produced a much higher R^2 of 0.8884. This higher fit value suggests diffusion-controlled transport through the nanogel network, where pH-dependent protonation may alter network swelling and apparent diffusional resistance, thereby changing the apparent diffusivity. At pH 5.0, the model fits for SUN release from SUN@CS-g-BOS yielded higher coefficients of determination than the corresponding fits at pH 7.4: 0.6955 for zero-order model, 0.7818 for the first-order model, and 0.9016 for the Higuchi model. Similarly, the Korsmeyer–Peppas model yielded the highest R^2 of 0.9659, indicating that it is the most suitable model at this pH. The Korsmeyer–Peppas model best described SUN release among the tested models. The release exponent (n) value calculated from the slope of the plot was 0.2772 at pH 7.4 and 0.3950 at pH 5.0 (Figure S2). Both values were <0.45, suggesting mainly Fickian diffusion. The fitting was carried out using the available release data. Because the Korsmeyer–Peppas model is most suitable for the initial release stage ($M_t/M_\infty \leq 0.6$), the results should be interpreted as suggesting a diffusion-controlled release mechanism rather than as conclusive evidence of purely Fickian transport. The kinetic analysis supports diffusion-mediated drug release at both pH values, with a better fit at pH 5.0. To provide perspective on the performance of SUN@CS-g-BOS compared with previously reported delivery platforms, Table 1 shows a summary of representative nanocarriers for sunitinib delivery in cancer treatment.

3.5. Cell Viability

The cytotoxicity of conditioned media generated from CS-g-BOS and SUN@CS-g-BOS formulations was evaluated in A549 and NIH3T3 cells. Cells exposed to conditioned media from blank CS-g-BOS formulations maintained >70% viability in NIH3T3 cells after 48 h (Figure 6F,G). A dose-dependent antiproliferative response was observed after exposure to conditioned media from SUN@CS-g-BOS formulations, as illustrated in Figure 6H–K. For conditioned media from SUN@CS-g-BOS, A549 cell viability decreased below 90% at concentrations of 1 and 2.5 μg/mL and reached 46% at 10 μg/mL after 48 h. Cell viability declined substantially above 15 μg/mL and

Table 1. Overview of Sunitinib-Loaded Nanocarriers for Cancer Treatment

cancer type	carrier type	particle size (nm)	zeta potential (mV)	EE	drug release	in vitro/in vivo effects	ref.
colon cancer	poly(lactic-co-glycolic acid) (PLGA)-based nanoparticles	132	−38	52%	91% in 48h	greater cytotoxicity than the free drug against HT-29 cells.	39
lung cancer	poly(3-hydroxybutyrate-co-3-hydroxyvalerate) (PHBV) nanoparticles	167.80	−1.37 ± 0.24	93.25 ± 0.03%	56% in 24h	unchanged cytotoxicity of sunitinib-loaded nanoparticles.	40
breast cancer	Lipoid-90H and chitosan	440	+34 ± 5.3	83.03%	84.11% in 48h	potent cytotoxicity in MCF-7 breast cancer cells	41
liver cancer	amphiphilic polymer (Ce6-PEG2000-FA)	58	+26	N/A	N/A	dose-dependent cytotoxicity, tumor fluorescence and photothermal imaging, inhibition of tumor growth, and complete eradication of tumors by laser irradiation.	42
leukemia	TPP-crosslinked hydroxypropyl methylcellulose (mHPMC)/chitosan nanocarriers	33 ± 5	N/A	up to 86%	93% and 44% in 48 h at pH 4.5 for low and high chitosan contents	dose-dependent cytotoxicity against leukemic cells.	43
leukemia	magnetic sepiolite (mSep) nanoparticles coated with chitosan	210–980	+4–+17	45 and 83%	76.2%, 68.2%, and 56.6% at pH 5.5 in 48 h	dose-dependent toxicity against leukemic cells, IC_{50} of 4 μg/mL.	44
lung cancer	CS-g-BOS nanogels	176.6	+8.3	95.52% (optimized 1:1 carrier-to-drug formulation)	70.03% at pH 5.0 and 13.35% at pH 7.4 after 432 h	dose-dependent cytotoxicity of conditioned media against A549 cells; IC_{50} = 5.8 ± 0.6 μg/mL after 48 h.	this work

https://doi.org/10.1021/acsami.6c02925
ACS Appl. Mater. Interfaces 2026, 18, 47237−47256

reached its minimum at 100 μg/mL (7.74%). The IC_{50} value for conditioned media from SUN@CS-g-BOS nanogels was 5.8 ± 0.6 μg/mL in A549 cells after 48 h (Figure 6K). The MTT heatmap shows the viability of A549 and NIH3T3 cells after 24 and 48 h of treatment with CS-g-BOS and SUN@CS-g-BOS formulations (Figure S3). Red indicates higher viability, whereas purple indicates higher toxicity. The heatmap shows the concentration-dependent cytotoxic activity of conditioned media from SUN@CS-g-BOS formulations against A549 cells. Representative cellular images of A549 and NIH3T3 cells after 48 h of treatment with conditioned media from CS-g-BOS and SUN@CS-g-BOS formulations are shown in Figure S4.

3.6. Flow Cytometry

Annexin V-FITC/PI staining was used to distinguish viable, early apoptotic, late apoptotic, and necrotic A549 cells. The untreated control group showed 99.2% viable cells (Q4), whereas treatment with CS-g-BOS, free SUN, and SUN@CS-g-BOS increased apoptotic populations to different extents (Figure 7D–F). CS-g-BOS nanogels induced only low levels of apoptosis under the tested conditions. The Q2 and Q3 regions, corresponding to late- and early-apoptotic cells, respectively, were used to estimate the total apoptotic population. At the IC_{50} concentration of SUN@CS-g-BOS, the formulation significantly increased the percentage of apoptotic A549 cells compared with the untreated

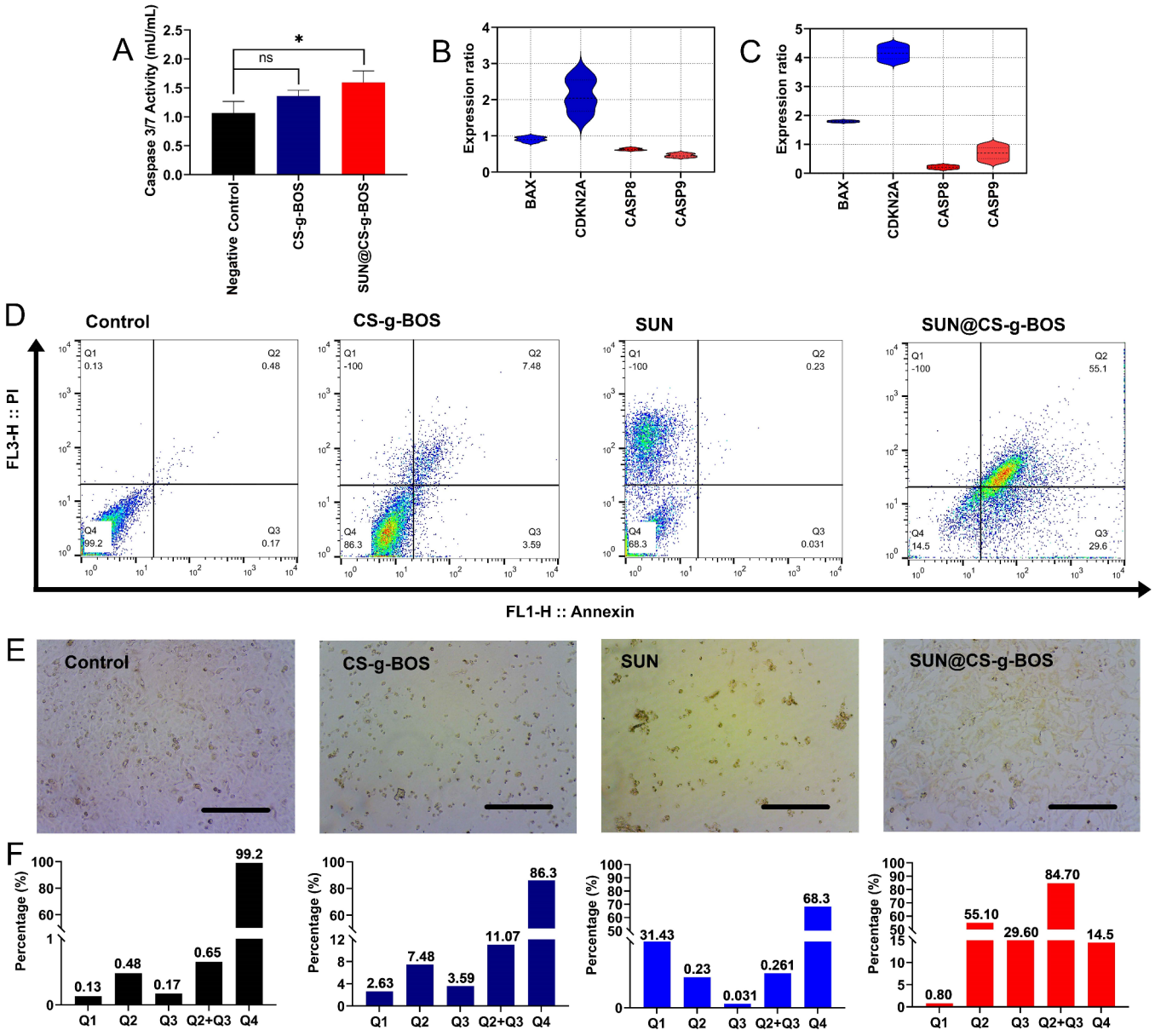


Figure 7. Evaluation of apoptotic activity and gene expression following different treatments. (A) Caspase-3/7 activity assay in the control, CS-g-BOS, and SUN@CS-g-BOS groups, indicating increased apoptosis (*$p < 0.05$). (B, C) RT-qPCR analysis of BAX, CDKN2A, CASP8, and CASP9 expression in treated A549 cells. Relative expression levels were normalized to B2M as the internal reference gene and calculated using the $2^{-\Delta\Delta Ct}$ method. Data are presented as mean ± SD; *$p < 0.05$. (D) Flow cytometry analysis of control, CS-g-BOS, SUN, and SUN@CS-g-BOS. (E) Microscopic images of treated cells stained for apoptosis-related morphology. (F) Quantification of apoptotic cell populations (Q1: necrotic, Q2: late apoptotic, Q3: early apoptotic, and Q4: viable).

https://doi.org/10.1021/acsami.6c02925
ACS Appl. Mater. Interfaces 2026, 18, 47237−47256

control and CS-g-BOS-treated groups. The total apoptotic population in the SUN@CS-g-BOS nanogel group was 84.70%.

3.7. Caspase Activity

Caspases are key mediators of apoptosis and play central roles in the execution of programmed cell death. Among them, caspase-8 and caspase-9 are associated with the extrinsic and intrinsic apoptotic pathways, respectively, whereas caspase-3 and caspase-7 function as downstream executioner caspases.[45,46] In this study, caspase-3/7 activity increased in the SUN-treated group compared with the control group, indicating SUN-induced apoptosis (Figure 7A). The highest caspase-3/7 activity was observed in the SUN@CS-g-BOS group, suggesting that CS-g-BOS nanogels enhanced the pro-apoptotic effect of SUN under the tested conditions. Similarly, Ahmed et al. reported increased caspase-3, caspase-9, and p53 levels in SUN-loaded lipid–polymer hybrid nanoparticle-treated MCF-7 cells compared with untreated controls, supporting apoptosis induction by SUN-based nanocarrier systems.[41]

3.8. Analysis of Apoptotic Gene Expression Using RT-qPCR

The relative mRNA expression levels of apoptosis-related target genes, including BAX, CDKN2A, CASP8, and CASP9, were assessed in treated A549 cells using RT-qPCR, with B2M as the internal reference gene. Figure 7B shows the relative expression levels of BAX, CDKN2A, CASP8, and CASP9 in A549 cells exposed to CS-g-BOS nanogels for 24 h. CDKN2A expression was higher than that of the other analyzed genes, suggesting that CDKN2A may contribute to the cellular response to CS-g-BOS treatment, whereas BAX, CASP8, and CASP9 showed relatively low expression levels. In SUN@CS-g-BOS-treated cells, CASP9 expression was markedly higher than that of BAX, CDKN2A, and CASP8 (Figure 7C). This increase in CASP9 expression suggests that SUN@CS-g-BOS may preferentially activate the intrinsic apoptotic pathway, in which caspase-9 plays a central role. Overall, these findings indicate that SUN@CS-g-BOS treatment modulated apoptosis-related gene expression and promoted programmed cell death in A549 cells under the tested conditions.

3.9. Microscopic Analysis of Stained Cells

Figure 8A presents fluorescence microscopy results for the control, SUN, and SUN@CS-g-BOS groups. DAPI staining, shown in blue in the first column, identifies nuclei. The second column shows PI (propidium iodide) staining, which marks dead or membrane-compromised cells because PI enters cells after loss

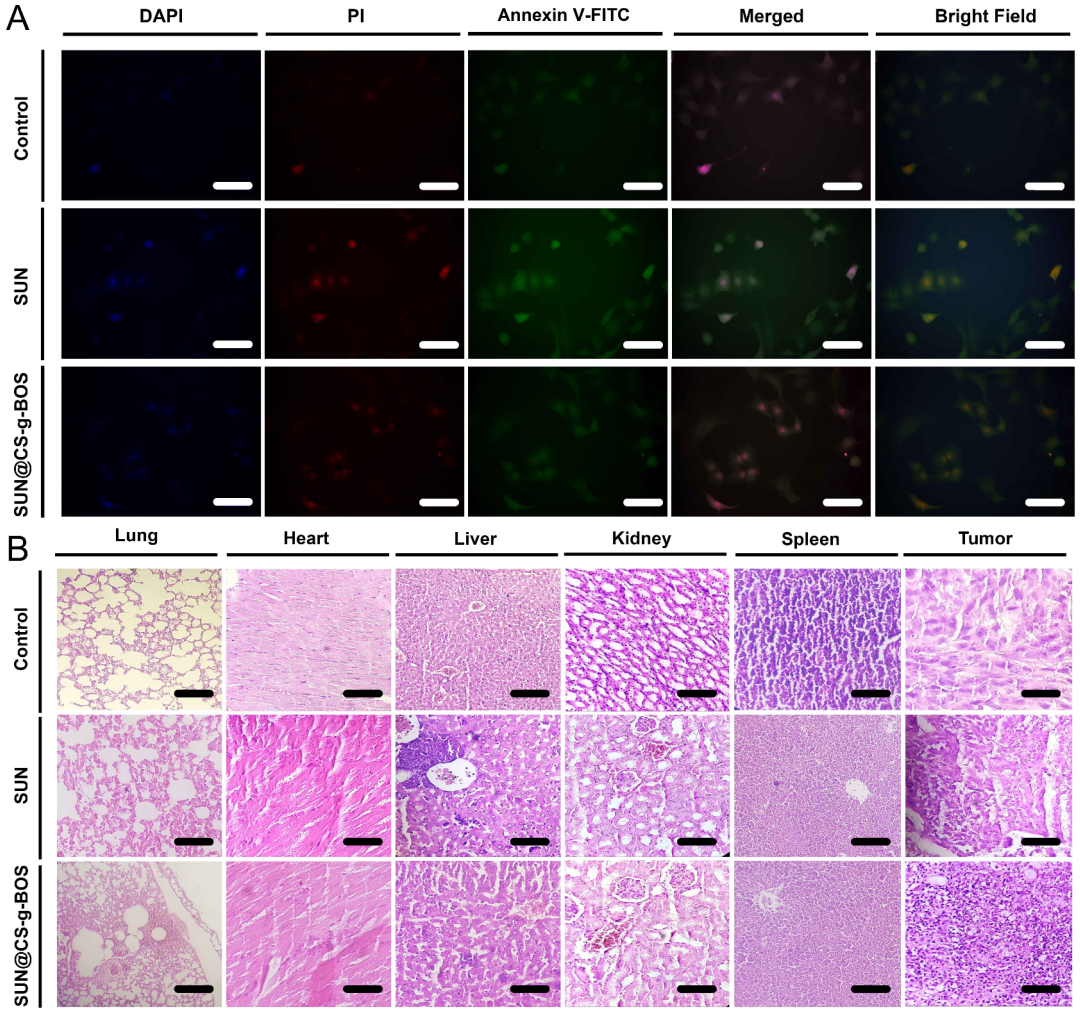


Figure 8. (A) Triple fluorescent labeling using DAPI, Annexin V, and PI. A549 cells were treated with fresh medium as the control, free SUN, or SUN@CS-g-BOS. (B) Histological examination of different organs (lung, heart, liver, kidney, spleen, and tumor) in the control, SUN, and SUN@CS-g-BOS groups. Scale bars = 50 μm.

https://doi.org/10.1021/acsami.6c02925
ACS Appl. Mater. Interfaces 2026, 18, 47237−47256

of plasma membrane integrity and binds DNA.[45] The cells were also stained with Annexin V-FITC, which fluoresces green upon binding to phosphatidylserine exposed on the outer leaflet of the plasma membrane during early apoptosis. In the control group, cells showed intact nuclei and minimal PI staining, indicating that most cells were viable. The SUN-treated group showed stronger PI staining than the control group, indicating increased cell death or membrane damage. SUN@CS-g-BOS-treated cells showed a stronger Annexin V-FITC signal, indicating enhanced phosphatidylserine exposure and apoptosis-associated membrane changes in treated cells. The staining pattern suggests greater membrane damage or late apoptosis in the SUN-loaded nanogel group than in the control group, as indicated by increased PI staining. The merged images show overlapping Annexin V- and PI-positive regions, suggesting a higher proportion of late-apoptotic or membrane-compromised cells following SUN@CS-g-BOS treatment. These staining results support apoptosis induction and membrane damage after SUN@CS-g-BOS treatment, but they do not provide direct evidence of nanogel uptake or internalization.

3.10. Histological Analysis

Figure 8B presents histological images and analysis of organ sections (lung, heart, liver, kidney, spleen, and tumor) for the control, SUN, and SUN@CS-g-BOS groups. Tissues from the control group exhibited normal histological architecture, intact cellular structures, and no obvious pathological alterations. The lungs showed well-defined alveoli; the myocardial tissue appeared normal; hepatic architecture was preserved, with clearly organized hepatocytes; and the kidneys showed normal glomeruli and tubules. The spleen showed normal white and red pulp, and the tumor tissue showed no extensive necrosis or apparent damage. In the SUN and SUN@CS-g-BOS groups, the spleen showed normal white and red pulp, and myocardial tissue appeared similar to that of the control group. The kidney tissue in the SUN and SUN@CS-g-BOS groups exhibited mild structural alterations compared with the control group. Compared with the control group, the SUN and SUN@CS-g-BOS groups showed severe hepatic inflammation, feathery degeneration, and necrosis, along with pulmonary congestion and pneumocyte hyperplasia. Across tumor sections from the control, SUN, and SUN@CS-g-BOS groups, malignant cells with hyperchromatic, irregular nuclei and eosinophilic cytoplasm were observed in sheets, with occasional mitotic figures, confirming the presence of tumor tissue in all groups. Tumor-volume data, together with histological confirmation of tumor tissue, support the antitumor activity of SUN@CS-g-BOS. However, histological analysis showed preserved heart and spleen morphology but revealed alterations in the liver, lungs, and kidneys, suggesting that systemic safety requires further optimization.

3.11. Scratch Assay

Figure 9A shows scratch assay images over time ($T = 0$, 12, and 24 h) for the control, CS-g-BOS, free SUN, and SUN@CS-g-BOS groups. In all groups, a clear cell-free gap was observed at $T = 0$. In the control group, the scratch remained mostly open, with approximately 18% closure after 12 h and 25% closure after 24 h, indicating limited spontaneous 3T3 fibroblast migration under the tested conditions. In contrast, the CS-g-BOS group showed greater scratch closure, reaching approximately 40% at 12 h and nearly 80% at 24 h. This enhanced closure may be associated with a more supportive microenvironment provided by the CS-g-BOS hydrogel precursor specimens, which may have promoted 3T3 fibroblast migration and/or proliferation. The free SUN group showed moderate scratch closure of approximately 30% at 12 h, which increased to approximately 40% by 24 h. The SUN@CS-g-BOS group also showed greater scratch closure than the control group, although closure remained lower than that observed in the CS-g-BOS group. Therefore, these data should be interpreted cautiously and primarily indicate that the tested treatments did not prevent 3T3 fibroblast migration and/or scratch closure under the assay conditions. The closure observed in the SUN-containing groups may reflect the matrix-supportive contribution of the CS-g-BOS-based environment and/or concentration-dependent effects of released components, rather than a direct SUN-mediated cytostatic effect in this fibroblast scratch model.[47]

3.12. In Vivo Analysis

Figure 9B–E show the in vivo effects of different treatments on tumor growth and body weight in mice. Photographs of mice and excised tumors indicated that tumors in the control group were larger than those in the SUN and SUN@CS-g-BOS groups (Figure 9B). A marked reduction in tumor size was observed in both the SUN and SUN@CS-g-BOS groups. Quantitative tumor-volume analysis (Figure 9C) supported this trend: tumor volume in the control group continued to increase over 11 days, reaching 1098 mm^3. CS-g-BOS slightly inhibited tumor growth, with tumor volume reaching approximately 862 mm^3 on day 11. In contrast, SUN significantly inhibited tumor growth, maintaining the volume below 500 mm^3, while SUN@CS-g-BOS produced similar suppression, with the tumor volume remaining below 500 mm^3. These data suggest that SUN and SUN@CS-g-BOS both suppress tumor growth relative to the control, and that nanogel delivery maintains antitumor efficacy while providing sustained-release behavior.

Body weight data are shown in Figure 9D as a nonspecific measure of systemic toxicity. The CS-g-BOS group showed stable or slightly increased body weight during treatment, indicating good biocompatibility. However, the control, SUN, and SUN@CS-g-BOS groups exhibited a small reduction in body weight, which may reflect disease burden and/or low-level drug-related toxicity. Although weight loss was not statistically significant, the formulation was well tolerated under the tested conditions. Figure 9E illustrates the tumor-to-body weight (BW) ratio, which can serve as a measure of treatment efficacy relative to systemic burden. The control group showed the highest tumor/BW ratio (59%), which indicates a high tumor burden relative to body weight. CS-g-BOS, SUN, and SUN@CS-g-BOS showed a significantly lower tumor/BW ratio compared with the control. SUN and SUN@CS-g-BOS showed the lowest ratio, indicating stronger therapeutic effects. All reductions were statistically significant ($p < 0.0001$), confirming that the treatments reduced tumor burden; however, organ histology indicates that systemic safety requires further optimization. These results suggest that SUN@CS-g-BOS may serve as a potential drug delivery system for tumor inhibition while maintaining an acceptable safety profile under the tested conditions.

3.13. CAM Assay

The antiangiogenic effect of SUN@CS-g-BOS was evaluated using the chick chorioallantoic membrane (CAM) assay

https://doi.org/10.1021/acsami.6c02925
ACS Appl. Mater. Interfaces 2026, 18, 47237−47256

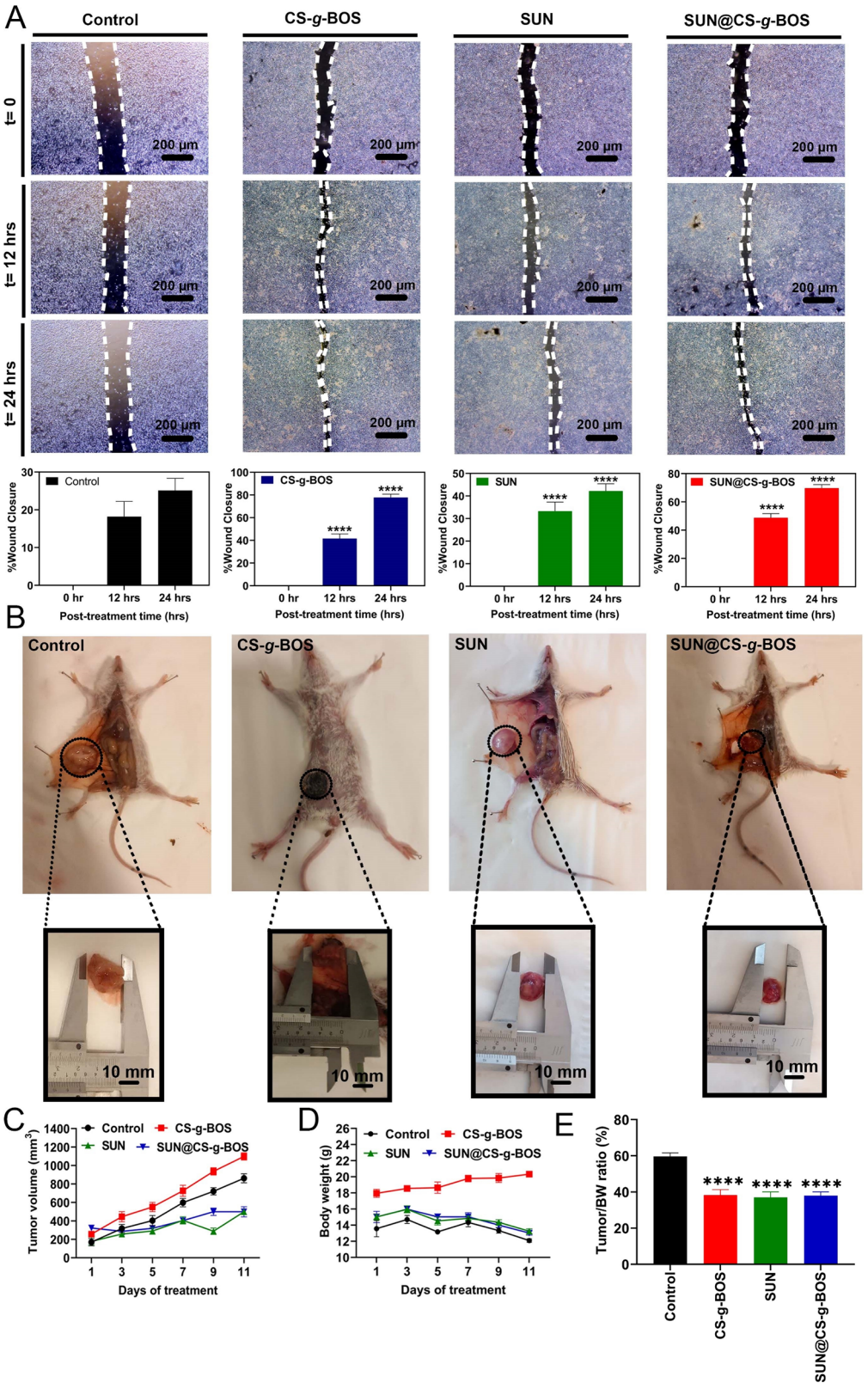


Figure 9. (A) Scratch assay images of the scratch-closure process over time (T = 0, 12, and 24 h) for control, CS-g-BOS, SUN, and SUN@CS-g-BOS. (B) Representative photographs of the treated mice and excised tumors after 11 days of treatment. The control group was untreated, whereas the other three experimental groups received CS-g-BOS, SUN, or SUN@CS-g-BOS. (C) Tumor volumes over time. (D) Body-weight changes. (E) Tumor-to-body-weight ratios.

https://doi.org/10.1021/acsami.6c02925
ACS Appl. Mater. Interfaces 2026, 18, 47237−47256

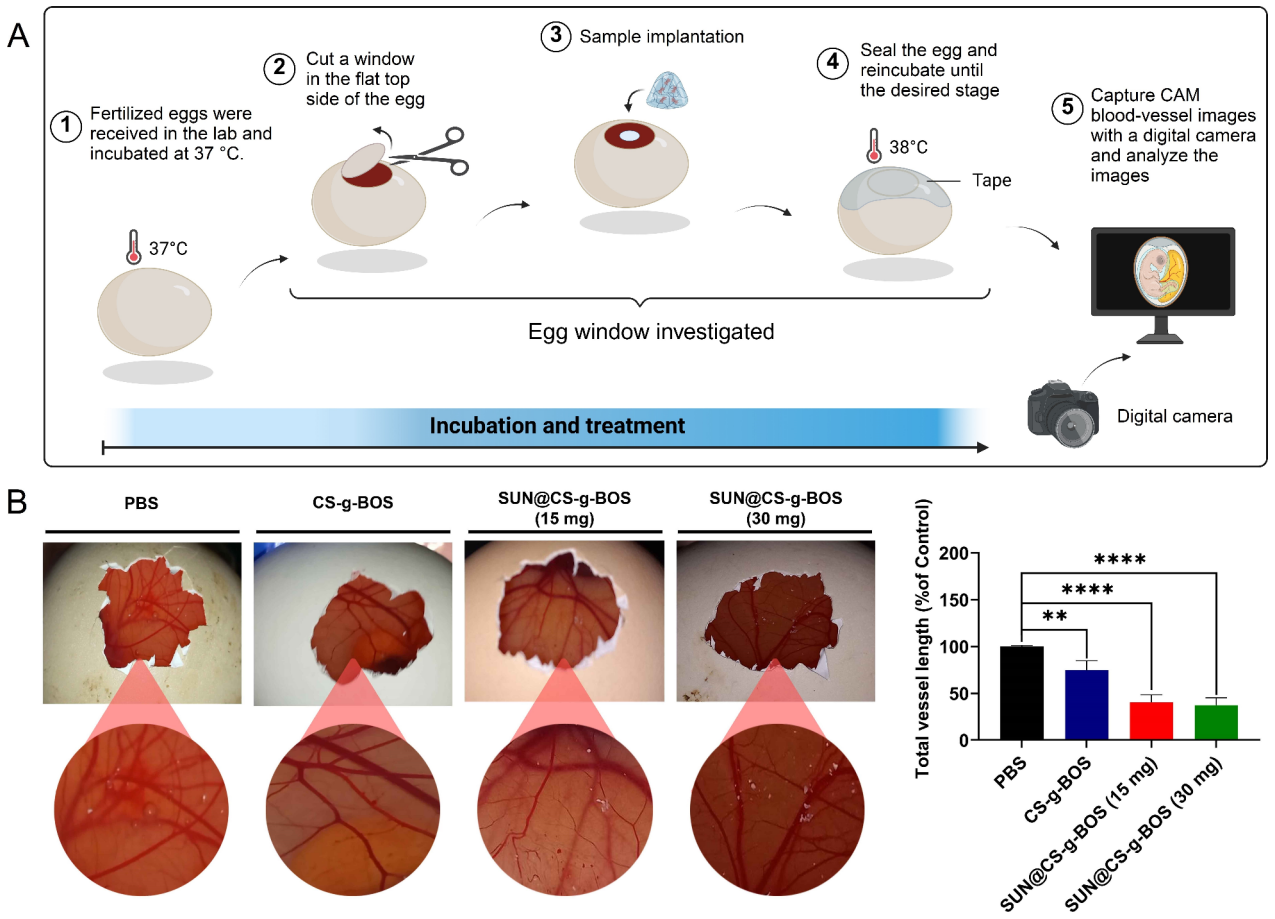


Figure 10. (A) Schematic of the chick chorioallantoic membrane (CAM) angiogenesis assay used as a complementary antiangiogenic screening model. (B) Photographs of CAMs treated with PBS (control), CS-g-BOS, and SUN@CS-g-BOS formulations at 15 mg and 30 mg. Magnified views highlight vascular density differences among groups. (C) Quantification of total vessel length, expressed as a percentage of the PBS control. Treatment with SUN@CS-g-BOS significantly reduced blood vessel formation in a dose-dependent manner. Data are presented as mean ± SD (**$p < 0.01$, ****$p < 0.0001$).

(Figure 10A). Angiogenesis was assessed on day 14 after treatment on embryonic day 8. The PBS control group displayed extensive vascular branching, whereas the CS-g-BOS group showed a modest reduction in vessel formation. Treatment with SUN@CS-g-BOS at 15 and 30 mg per CAM reduced total vessel length compared with the control (Figure 10B). Quantitative analysis of total vessel length confirmed a significant decrease in angiogenesis in the SUN@CS-g-BOS-treated groups compared with the PBS control (Figure 10C). These total formulation masses were selected based on preliminary optimization and are reported as the total formulation mass applied per CAM. The observed antiangiogenic effect is consistent with the established role of SUN as a tyrosine kinase inhibitor that targets angiogenesis-related receptors, including VEGFR and PDGFR. Overall, the CAM results indicate that SUN@CS-g-BOS effectively suppresses new blood vessel formation under the tested conditions.

4. CONCLUSIONS

In this work, we developed a bio-derived, pH-responsive chitosan nanogel platform in which boswellic acid functions as a dual-purpose bioactive network modifier for controlled drug transport. Chitosan–BOS (CS-g-BOS) hydrogel precursors were synthesized by formaldehyde-assisted network formation and subsequently converted into CS-g-BOS nanogels by STPP-mediated ionic condensation. Extensive characterization using ^{1}H NMR, FTIR, SEM, AFM, DLS, zeta potential, TGA, and rheology supported the formation of a porous, shear-thinning hydrogel precursor and stable hydrogel-derived nanostructures. SUN loading into CS-g-BOS nanogels achieved a high encapsulation efficiency (95.52%), highlighting the strong affinity of the engineered network for drug retention. The CS-g-BOS network provided sustained and pH-dependent release over an extended period, reaching 70.03% cumulative SUN release at pH 5.0 compared with 13.35% at pH 7.4 after 432 h, demonstrating that environmental pH modulates swelling and transport pathways within the nanogel matrix. Kinetic fitting suggested diffusion-mediated transport behavior described by the Korsmeyer–Peppas model, consistent with release governed primarily by molecular diffusion through the responsive network rather than rapid depletion. Biological evaluation further validated the material platform's delivery performance. Conditioned media from SUN@CS-g-BOS nanogels showed dose-dependent cytotoxicity against A549 cells (IC_{50} = 5.8 ± 0.6 μg/mL at 48 h) as measured by the MTT assay and induced a high apoptotic population (84.70%) based on flow cytometry, with apoptosis further supported by caspase-3/7

https://doi.org/10.1021/acsami.6c02925
ACS Appl. Mater. Interfaces 2026, 18, 47237−47256

activation, apoptosis-related gene-expression changes, and Annexin V/PI/DAPI staining. Separately, a scratch-closure analysis in 3T3 fibroblasts indicated that the tested formulations did not prevent fibroblast migration and/or scratch closure under the tested conditions. In vivo studies in a mouse tumor model indicated that SUN@CS-g-BOS reduced tumor volume, and CAM assays demonstrated antiangiogenic activity, supporting the conclusion that the nanogel formulation preserved therapeutic activity while enabling sustained, pH-dependent delivery. The in vitro concentrations used in this study were selected based on IC_{50} and dose-response analyses in A549 cells, and the in vivo dose was chosen according to tolerability and previously reported therapeutic ranges for SUN-based formulations, thereby supporting preliminary cross-model relevance between cellular and animal studies. Overall, these results establish CS-g-BOS nanogels as a scalable, bio-derived materials-design strategy that integrates network engineering with pH-responsive transport control for sustained anticancer drug delivery.

■ ASSOCIATED CONTENT

Data Availability Statement

Data will be made available on request.

Supporting Information

The Supporting Information is available free of charge at https://pubs.acs.org/doi/10.1021/acsami.6c02925.

The Supporting Information includes Table S1 listing the real-time PCR primer sequences used in this study, along with additional characterization and biological data: dynamic light scattering size distributions for CS-g-BOS and SUN@CS-g-BOS nanogels and their corresponding zeta potentials (Figure S1); kinetic model fits (Korsmeyer–Peppas, Higuchi, first-order, and zero-order) for SUN release at pH 7.4 and 5.0 (Figure S2); an MTT heatmap summarizing cell viability for A549 and NIH3T3 cells after 24 and 48 h of exposure to conditioned media from CS-g-BOS and SUN@CS-g-BOS formulations (Figure S3); and representative cellular images of A549 and NIH3T3 cells after 48 h of treatment with CS-g-BOS and SUN@CS-g-BOS (Figure S4) (DOCX)

■ AUTHOR INFORMATION

Corresponding Authors

Zahra Haghighatian – *Department of Pathology, School of Medicine, Lorestan University of Medical Sciences, Khorramabad 6813833946, Iran;* Email: Haghighatian14@yahoo.com

Yavuz Nuri Ertas – *Department of Biomedical Engineering, Erciyes University, Kayseri 38039, Türkiye;* orcid.org/0000-0002-6791-7484; Email: yavuznuri@gmail.com

Bahareh Farasati Far – *Department of Biomedical Engineering, Erciyes University, Kayseri 38039, Türkiye;* orcid.org/0000-0002-1598-2487; Email: bahar.ferasati@gmail.com

Authors

Zahra Amiri – *Department of Medical Nanotechnology, School of Medicine, North Khorasan University of Medical Sciences, Bojnurd 94149, Iran*

Mehdi Jahanbakhshi – *School of Chemical Engineering, College of Engineering, University of Tehran, Tehran 1417935840, Iran;* orcid.org/0000-0001-9901-5250

Mohsen Momeni – *Cancer Metabolism and Tumor Microenvironment Group, Laboratory of Tumor and Development Biology, GIGA-Cancer, University of Liège, Liège 4000, Belgium*

Ehsan Heidary – *Department of Infectious Diseases and Geographic Medicine, Stanford University School of Medicine, Stanford, CA 94305, United States of America*

Shaghayegh AdibAmini – *Plasma Physics Research Center, Science and Research Branch, Islamic Azad University, Tehran 1477893855, Iran;* orcid.org/0000-0002-3357-556X

Tara Hassani Goodarzi – *Jiann-Ping Hsu College of Public Health, Georgia Southern University, Statesboro, GA 30460, United States of America*

Arian Karimi Rouzbahani – *Surgery Education and Researching Network (SERGN), Universal Scientific Education and Research Network (USERN), Khorramabad 6813833946, Iran*

Complete contact information is available at: https://pubs.acs.org/doi/10.1021/acsami.6c02925

Funding

This research did not receive any specific grant from funding agencies in the public, commercial, or not-for-profit sectors.

Notes

All animal procedures were approved by the Animal Ethics and Research Committee of Lorestan University of Medical Sciences (IR.LUMS.REC.1404.235) and complied with the National Committee for Ethics in Biomedical Research guidelines.
The authors declare no competing financial interest.

■ ACKNOWLEDGMENTS

Y.N.E. acknowledges support from the Health Institutes of Türkiye (TÜSEB) Incentive Award, the Turkish Academy of Sciences Distinguished Young Scientist Award (TÜBA-GEBİP), and the Scientific and Technological Research Council of Türkiye (TÜBİTAK) Incentive Award. During the preparation of this manuscript, the authors used Grammarly and ChatGPT to improve language clarity and grammar. The authors reviewed and edited the content as necessary and take full responsibility for the final content.

■ REFERENCES

(1) Kubeil, M.; Suzuki, Y.; Casulli, M. A.; Kamal, R.; Hashimoto, T.; Bachmann, M.; Hayashita, T.; Stephan, H. Exploring the Potential of Nanogels: From Drug Carriers to Radiopharmaceutical Agents. *Adv. Healthcare Mater.* **2024**, *13* (1), No. 2301404.

(2) Fatima, M.; Almalki, W. H.; Khan, T.; Sahebkar, A.; Kesharwani, P. Harnessing the Power of Stimuli-Responsive Nanoparticles as an Effective Therapeutic Drug Delivery System. *Adv. Mater.* **2024**, *36* (24), No. 2312939.

(3) Taherinazam, A.; Entezari, M.; Firouz, Z. M.; Hajimazdarany, S.; Heydargoy, M. H.; Moghadassi, A. H. A.; Moghadaci, A.; Sadrani, A.; Motahhary, M.; Nashtifani, A. H.; et al. Eco-friendly chitosan-based nanostructures in diabetes mellitus therapy: Promising bioplatforms with versatile therapeutic perspectives. *Environ. Res.* **2023**, *228*, No. 115912.

(4) Yu, Q. Y.; Gao, Y.; Dai, W. C.; Li, D. N.; Zhang, L.; Hameed, M. M. A.; Guo, R.; Liu, M.; Shi, X. Y.; Cao, X. Y. Cell Membrane-Camouflaged Chitosan-Polypyrrole Nanogels Co-Deliver Drug and Gene for Targeted Chemotherapy and Bone Metastasis Inhibition of Prostate Cancer. *Adv. Healthcare Mater.* **2024**, *13* (20), No. 2400114.

(5) Chen, X. J.; Wu, D.; Chen, Z. Biomedical applications of stimuli-responsive nanomaterials. *Medcomm* **2024**, *5* (8), No. e643.
(6) Karimi, K.; Mojtabavi, S.; Tehrany, P. M.; Nejad, M. M.; Rezaee, A.; Mohtashamian, S.; Hamedi, E.; Yousefi, F.; Salmani, F.; Zandieh, M. A.; et al. Chitosan-based nanoscale delivery systems in hepatocellular carcinoma: Versatile bio-platform with theranostic application. *Int. J. Biol. Macromol.* **2023**, *242*, No. 124935.
(7) Campea, M. A.; Lofts, A.; Xu, F.; Yeganeh, M.; Kostashuk, M.; Hoare, T. Disulfide-Cross-Linked Nanogel-Based Nanoassemblies for Chemotherapeutic Drug Delivery. *ACS Appl. Mater. Interfaces* **2023**, *15* (21), 25324–25338.
(8) Ghiorghita, C.-A.; Platon, I.-V.; Lazar, M. M.; Dinu, M. V.; Aprotosoaie, A. C. Trends in polysaccharide-based hydrogels and their role in enhancing the bioavailability and bioactivity of phytocompounds. *Carbohydr. Polym.* **2024**, *334*, No. 122033.
(9) Li, T. F.; Ashrafizadeh, M.; Shang, Y. R.; Ertas, Y. N.; Orive, G. Chitosan-functionalized bioplatforms and hydrogels in breast cancer: immunotherapy, phototherapy and clinical perspectives. *Drug Discovery Today* **2024**, *29* (1), No. 103851.
(10) Omrani, M.; Naimi-Jamal, M. R.; Far, B. F. The design of multi-responsive nanohydrogel networks of chitosan for controlled drug delivery. *Carbohydr. Polym.* **2022**, *298*, No. 120143.
(11) Farasati Far, B.; Omrani, M.; Naimi Jamal, M. R.; Javanshir, S. Multi-responsive chitosan-based hydrogels for controlled release of vincristine. *Commun. Biochem.* **2023**, *6* (1), No. 28.
(12) Roy, N. K.; Parama, D.; Banik, K.; Bordoloi, D.; Devi, A. K.; Thakur, K. K.; Padmavathi, G.; Shakibaei, M.; Fan, L.; Sethi, G.; Kunnumakkara, A. B. An Update on Pharmacological Potential of Boswellic Acids against Chronic Diseases. *Int. J. Mol. Sci.* **2019**, *20*, No. 4101.
(13) Huang, G.; Yang, J.; Zhang, L.; Cao, L.; Zhang, M.; Niu, X.; Zhou, Z.; Zhang, X.; Li, P.; Liu, J. F. Inhibitory effect of 11-carbonyl-beta-boswellic acid on non-small cell lung cancer H446 cells. *Biochem. Biophys. Res. Commun.* **2018**, *503* (4), 2202–2205.
(14) Sanders, W. G.; Hogrebe, P. C.; Grainger, D. W.; Cheung, A. K.; Terry, C. M. A biodegradable perivascular wrap for controlled, local and directed drug delivery. *J. Controlled Release* **2012**, *161* (1), 81–89.
(15) Socinski, M. A.; Novello, S.; Brahmer, J. R.; Rosell, R.; Sanchez, J. M.; Belani, C. P.; Govindan, R.; Atkins, J. N.; Gillenwater, H. H.; Pallares, C.;et al.Multicenter, Phase II Trial of Sunitinib in Previously Treated, Advanced Non–Small-Cell Lung Cancer. *J. Clin. Oncol.* **2008**, *26* (4), 650–656.
(16) Houk, B. E.; Bello, C. L.; Kang, D.; Amantea, M. A Population Pharmacokinetic Meta-analysis of Sunitinib Malate (SU11248) and Its Primary Metabolite (SU12662) in Healthy Volunteers and Oncology Patients. *Clin. Cancer Res.* **2009**, *15* (7), 2497–2506.
(17) Faivre, S.; Delbaldo, C.; Vera, K.; Robert, C.; Lozahic, S.; Lassau, N.; Bello, C.; Deprimo, S.; Brega, N.; Massimini, G.; et al. Safety, Pharmacokinetic, and Antitumor Activity of SU11248, a Novel Oral Multitarget Tyrosine Kinase Inhibitor, in Patients With Cancer. *J. Clin. Oncol.* **2006**, *24* (1), 25–35.
(18) Shah, P.; Thomas, G. An Improved Process for Preparation and Purification of Boswellic Acids. WO2014195976A2, **2014**.
(19) Fahim, A. Z. M.; Ghouse, M. S.; Islam, S. Q.; Danish, M. A. M.; Mehmood, S.; Saniya, S.; Fatima, M. Q. I. Isolation and Identification of Boswellic Acids by Modern Analytical Techniques. *Asian J. Pharm. Anal. Med. Chem.* **2021**, *11* (2), 98–112.
(20) Zahid, A. A.; Ahmed, R.; Raza ur Rehman, S.; Augustine, R.; Tariq, M.; Hasan, A. Nitric oxide releasing chitosan-poly (vinyl alcohol) hydrogel promotes angiogenesis in chick embryo model. *Int. J. Biol. Macromol.* **2019**, *136*, 901–910.
(21) Nosrati, H.; Salehiabar, M.; Charmi, J.; Yaray, K.; Ghaffarlou, M.; Balcioglu, E.; Ertas, Y. N. Enhanced In Vivo Radiotherapy of Breast Cancer Using Gadolinium Oxide and Gold Hybrid Nanoparticles. *ACS Appl. Bio Mater.* **2023**, *6* (2), 784–792.
(22) Olfa, K.-Z.; José, L.; Salma, D.; Amine, B.; Najet, S. A.; Nicolas, A.; Maxime, L.; Raoudha, Z.; Kamel, M.; Jacques, M.; et al. Lebestatin, a disintegrin from Macrovipera venom, inhibits integrin-mediated cell adhesion, migration and angiogenesis. *Lab. Invest.* **2005**, *85* (12), 1507–1516.
(23) Farasati Far, B.; Jahanbakhshi, M.; Jameie, L.; Zolfigol, F.; Taromi, P.; Ertas, Y. N. Chitosan-graft-Pomegranate Extract Hydrogel: A Dual-Functional Pad for Antibacterial and Antioxidant Enhancement for Shelf Life Extension in Food Packaging. *ACS Appl. Polym. Mater.* **2024**, *6* (16), 9545–9558.
(24) Farasati Far, B.; Naimi-Jamal, M. R.; Jahanbakhshi, M.; Rostamani, H.; Karimi, M.; Keihankhadiv, S. Synthesis and characterization of chitosan/collagen/polycaprolactone hydrogel films with enhanced biocompatibility and hydrophilicity for artificial tendon applications. *Int. J. Biol. Macromol.* **2023**, *253*, No. 127448.
(25) Li, J.; Mooney, D. J. Designing hydrogels for controlled drug delivery. *Nat. Rev. Mater.* **2016**, *1* (12), No. 16071.
(26) Farasati Far, B.; Naimi-Jamal, M. R.; Jahanbakhshi, M.; Hadizadeh, A.; Dehghan, S.; Hadizadeh, S. Enhanced antibacterial activity of porous chitosan-based hydrogels crosslinked with gelatin and metal ions. *Sci. Rep.* **2024**, *14* (1), No. 7505.
(27) Farasati Far, B.; Naimi-Jamal, M. R.; Jahanbakhshi, M.; Khalafvandi, S. A.; Alian, M.; Razeghi Jahromi, D. Decontamination of Congo red dye from aqueous solution using nanoclay/chitosan-graft-gelatin nanocomposite hydrogel. *J. Mol. Liq.* **2024**, *395*, No. 123839.
(28) Lawrie, G.; Keen, I.; Drew, B.; Chandler-Temple, A.; Rintoul, L.; Fredericks, P.; Grøndahl, L. Interactions between Alginate and Chitosan Biopolymers Characterized Using FTIR and XPS. *Biomacromolecules* **2007**, *8* (8), 2533–2541.
(29) Joseph, J. J.; Sangeetha, D.; Gomathi, T. Sunitinib loaded chitosan nanoparticles formulation and its evaluation. *Int. J. Biol. Macromol.* **2016**, *82*, 952–958.
(30) Nasti, A.; Zaki, N. M.; deLeonardis, P.; Ungphaiboon, S.; Sansongsak, P.; Rimoli, M. G.; Tirelli, N. Chitosan/TPP and Chitosan/TPP-hyaluronic Acid Nanoparticles: Systematic Optimisation of the Preparative Process and Preliminary Biological Evaluation. *Pharm. Res.* **2009**, *26* (8), 1918–1930.
(31) Hamdi, M.; Hajji, S.; Affes, S.; Taktak, W.; Maâlej, H.; Nasri, M.; Nasri, R. Development of a controlled bioconversion process for the recovery of chitosan from blue crab (Portunus segnis) exoskeleton. *Food Hydrocolloids* **2018**, *77*, 534–548.
(32) Affes, S.; Aranaz, I.; Acosta, N.; Heras, Á.; Nasri, M.; Maalej, H. Chitosan derivatives-based films as pH-sensitive drug delivery systems with enhanced antioxidant and antibacterial properties. *Int. J. Biol. Macromol.* **2021**, *182*, 730–742.
(33) Huanbutta, K.; Cheewatanakornkool, K.; Terada, K.; Nunthanid, J.; Sriamornsak, P. Impact of salt form and molecular weight of chitosan on swelling and drug release from chitosan matrix tablets. *Carbohydr. Polym.* **2013**, *97* (1), 26–33.
(34) Gupta, R.; Swarupa, S.; Mayya, C.; Bhatia, D.; Thareja, P. Graphene Oxide–Carbamoylated Chitosan Hydrogels with Tunable Mechanical Properties for Biological Applications. *ACS Appl. Bio Mater.* **2023**, *6* (2), 578–590.
(35) Rostaminejad, B.; Karimi, A. R.; Dinari, M.; Hadizadeh, M. Photosensitive Chitosan-Based Injectable Hydrogel Chemically Cross-Linked by Perylene Bisimide Dopamine with Robust Antioxidant and Cytotoxicity Enhancer Properties for In Vitro Photodynamic Therapy of Breast Cancer. *ACS Appl. Bio Mater.* **2023**, *6* (3), 1242–1251.
(36) Kong, D.; Li, Y.; Yang, B.; Pang, Y.; Yuan, H.; Du, C.; Tan, Y. 3D-Printed Hydrogels with High-Strength and Anisotropy Mediated by Chain Rigidity. *Small* **2024**, *20* (44), No. 2403052.
(37) Far, B. F.; Jahanbakhshi, M.; Jameie, L.; Shojaei, A.; Zarei, K.; Taromi, P.; Jafarzadeh, S.; Ertas, Y. N. Chitosan-Graft-Gelatin Hydrogel Containing Bromothymol Blue as a Food Spoilage Indicator for Intelligent Food Packaging. *Adv. Mater. Interfaces* **2025**, *12* (9), No. 2400799.
(38) Yasuhara, K.; Kuroda, K. Kinetic study of all-or-none hemolysis induced by cationic amphiphilic polymethacrylates with antimicrobial activity. *Chin. Chem. Lett.* **2015**, *26* (4), 479–484.
(39) Alshetaili, A. S.; Anwer, M. K.; Alshahrani, S. M.; Alalaiwe, A.; Alsulays, B. B.; Ansari, M. J.; Imam, F.; Alshehri, S. Characteristics

https://doi.org/10.1021/acsami.6c02925
ACS Appl. Mater. Interfaces 2026, 18, 47237–47256

and anticancer properties of Sunitinib malate-loaded poly-lactic-co-glycolic acid nanoparticles against human colon cancer HT-29 cells lines. *Trop. J. Pharm. Res.* **2018**, *17* (7), 1263–1269.
(40) Otroj, M.; Taymouri, S.; Varshosaz, J.; Mirian, M. Preparation and characterization of dry powder containing sunitinib loaded PHBV nanoparticles for enhanced pulmonary delivery. *J. Drug Deliv. Sci. Tec.* **2020**, *56*, No. 101570.
(41) Ahmed, M. M.; Anwer, M. K.; Fatima, F.; Aldawsari, M. F.; Alalaiwe, A.; Alali, A. S.; Alharthi, A. I.; Kalam, M. A. Boosting the Anticancer Activity of Sunitinib Malate in Breast Cancer through Lipid Polymer Hybrid Nanoparticles Approach. *Polymers* **2022**, *14*, No. 2459.
(42) Xu, W.; Yang, M.; Du, X.; Peng, H.; Yang, Y.; Wang, J.; Zhang, Y. Multifunctional Nanoplatform Based on Sunitinib for Synergistic Phototherapy and Molecular Targeted Therapy of Hepatocellular Carcinoma. *Micromachines* **2023**, *14*, No. 613.
(43) Jafari, H.; Mahdavinia, G. R.; Kazemi, B.; Ehrlich, H.; Joseph, Y.; Rahimi-Nasrabadi, M. Highly efficient sunitinib release from pH-responsive mHPMC@Chitosan core-shell nanoparticles. *Carbohydr. Polym.* **2021**, *258*, No. 117719.
(44) Jafari, H.; Namazi, H.; Mahdavinia, G. R. pH-sensitive biocompatible chitosan/sepiolite-based cross-linked citric acid magnetic nanocarrier for efficient sunitinib release. *Int. J. Biol. Macromol.* **2023**, *242*, No. 124739.
(45) Dehghan, S.; Naghipour, A.; Anbaji, F. Z.; Golshanrad, P.; Mirazi, H.; Adelnia, H.; Bodaghi, M.; Far, B. F. Enhanced in vitro and in vivo anticancer activity through the development of Sunitinib-Loaded nanoniosomes with controlled release and improved uptake. *Int. J. Pharm.* **2023**, *640*, No. 122977.
(46) Shim, M. K.; Yoon, H. Y.; Lee, S.; Jo, M. K.; Park, J.; Kim, J.-H.; Jeong, S. Y.; Kwon, I. C.; Kim, K. Caspase-3/-7-Specific Metabolic Precursor for Bioorthogonal Tracking of Tumor Apoptosis. *Sci. Rep.* **2017**, *7* (1), No. 16635.
(47) Andrae, N.; Kirches, E.; Hartig, R.; Haase, D.; Keilhoff, G.; Kalinski, T.; Mawrin, C. Sunitinib targets PDGF-receptor and Flt3 and reduces survival and migration of human meningioma cells. *Eur. J. Cancer* **2012**, *48* (12), 1831–1841.

https://doi.org/10.1021/acsami.6c02925
ACS Appl. Mater. Interfaces 2026, 18, 47237–47256